Primary Productivity of Intertidal mudflats in the Wadden Sea: A Remote Sensing Method

TIMOTHY DUBE
February, 2012

SUPERVISORS:
Dr. Ir. Mhd. (Suhyb). Salama
Dr. Ir. C.M.M. (Chris). Mannaerts
INPLACE externals:
Dr. Eelke Folmer, NIOZ
Prof. Dr.Jacco Kromkamp

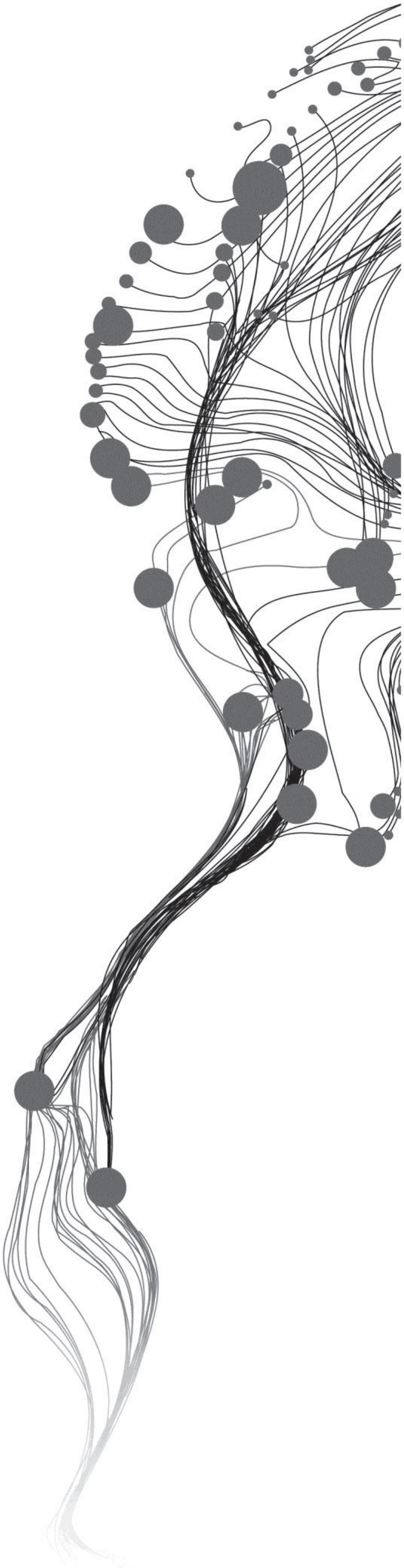

Primary Productivity of Intertidal mudflats in the Wadden Sea: A Remote Sensing Method

TIMOTHY DUBE
Enschede, The Netherlands, February 2012

Thesis submitted to the Faculty of Geo-Information Science and Earth Observation of the University of Twente in partial fulfilment of the requirements for the degree of Master of Science in Geo-information Science and Earth Observation.
Specialization: Water Resources and Environmental Management

SUPERVISORS:
Dr. Ir. Mhd. (Suhyb). Salama
Dr. Ir. C.M.M. (Chris). Mannaerts
INPLACE externals:
Dr. Eelke Folmer, NIOZ
Prof. Dr.Jacco Kromkamp

THESIS ASSESSMENT BOARD:
Prof. Dr. Ir. W. (Wouter), Verhoef (Chair)
Dr. Hans van der Woerd, (External examiner, Vrije Universiteit Amsterdam)

Abstract

The relative contribution of microphytobenthic (MPB) primary productivity to the total primary productivity of intertidal ecosystems is largely unknown. The possibility to estimate MPB primary productivity would be a significant contribution to a better understanding of the role of intertidal mudflats for ecosystem functioning. Estimation of MPB primary productivity from the exposed intertidal mudflats in the Dutch Wadden Sea, Netherlands was done following a two-step procedure. Firstly, supervised and image based classification methods were used to map classes of sediment types since sediment properties are important for MPB primary productivity. The two sediment classification methods were based on the Spectral Angle Mapper (SAM) algorithm using field collected and image extracted endmembers. Secondly, MPB primary productivity in the Dutch Wadden Sea was estimated following the model by Platt and Jassby (1976) for the top sediment layer (2 mm depth) using NDVI as a proxy for MPB biomass. Sensitivity analysis was also done using sediment euphotic depth of 2 mm, 5 mm and 7 mm; diffuse attenuation coefficient (Kd) of 1.61 and 2.60 mm^{-1} and photosynthetic efficiency (α^B) of 0.026 and 0.037 to assess their effect on intertidal mudflat MPB primary productivity. The results demonstrate that different sediment types have different spectral signatures produced by the presence of MPB organisms which have chl-*a* that absorbs at approximately 673 nm. In addition, the findings indicate that different sediment types can be characterised from remote sensing data using SAM algorithm, based on their spectral characteristics. The results further illustrate that derived clay and sand sediment classes from intertidal mudflats vary spatially and temporally. Again, derived chl-a+ phaeopigments concentration [mgm^{-2}] varied spatially and temporally and the distribution resembles that of clay and sand sediment classes characterized. High chl-a+ phaeopigments concentration [mgm^{-2}] were observed on areas with clay sediments and low in areas with sand. A significant linear relationship was found between maximum rate of photosynthesis at saturating irradiance (P^B_{max}) and land surface temperature with a coefficient of determination (R^2) of 0.71. The results also indicate that MPB primary productivity from intertidal mudflats sediments can be mapped using remote sensing methods. Estimated MPB primary productivity varied spatially and the distribution is similarly comparable to that of derived clay and sand sediment classes, with high MPB primary productivity found in clay sediments and limited amounts on sand. Sensitivity analysis results have shown that MPB primary productivity in mudflats is largely controlled by α^B, euphotic depth and Kd.

Keywords: Chl-*a*+ phaeopigments, Intertidal mudflats, Aqua, Microphytobenthic, Remote sensing, Primary productivity.

Acknowledgements

First and foremost, it is my pleasure to thank my first supervisor Dr. Suhyb Salama for the steadfast support and supervision, which was always the deriving and motivational spirit that kept me working on this thesis. When I faced scientific problems his door was always wide open for me; no matter how complex problems were; the moment we discussed, he made me realise my potential. Surely, he taught me how to do science and be an independent researcher. I was personal not confident with hydro-optic concepts but rather approached tasks with fear and doubt but he kept on saying, "Timothy keep on trying I know you can do it."

Secondly, would like to extend my sincere appreciation to my second supervisor Dr. Chris Mannaerts for the guidance and support in fine tuning my ideas as well as critically reviewing my work. To Dr. Eelke Folmer my external supervisor, it was a great opportunity working with you, not forgetting the critical but rather constructive ideas and comments from an eco-hydrological perspective you always raised.

I would like to thank the Navicula and IN PLACE teams from the Royal Netherlands Institute for Sea Research (NIOZ) and ITC for their technical and scientific supports. Thanks to Katja Philippart (NIOZ) and Jacco Kromkamp (NIOZ-Yerseke) for allowing me to use IN PLACE and NIOZ facilities. Field data of this research was collected during the NAV09 cruise as part of the Integrated Network for Productivity and Loss Assessment in the Coastal Environment, the IN PLACE project. To Jacco Kromkamp I say, "You played a very big part for this thesis to be a success, thank you once again for sharing your scientific expertise with me."

I would like to thank the European Space Agency (ESA) for providing full resolution Meris images over the Wadden Sea. It's my pleasure as well to extend a word of thanks to Ben Maathuis and ITC supporting team for facilitating the retrieval of Meris images via the GEONETCast system. To Petra Budde, Web coordinator of the ITC RSG lab, thank you for quick response in retrieving Landsat and Aster images.

More so, I would also like to thank the Water Resources Department staff, ITC library for the different roles they played during the whole period of my study at ITC. To WREM 2010-2012 students and my environmental hydrology colleagues, you were the best team guys to work with. To Micael Woldegiorgis (Eritrea), Sudha Shrestha (Nepal) my fieldwork teammates and friends, your companionship was great. Ugyen Eden (Bhutan), Tinebeb Yohannes (Ethiopia) and David (Rwanda) my friends, thank you for the time and the academic ideas we shared. To the ITC fellowship, thank you for being a home away from home. I would also like to thank all my friends and colleagues from Geography and Environmental Science Department for the support. Many thanks go to Cletah for the courageous support and prayers throughout the whole period of my study, surely that was wonderful. A word of thanks also goes to the Zimbabwean community at ITC particularly Mary, Tsitsi Bangira and Terence; it was great being together.

Special thanks also go to Mr and Mrs Dube, my parents and my family for the love, moral support, encouragement and care they showed. To my sister Lisbeth, you played a very a big role in my life.

Finally, I would like to thank the Dutch government for granting me with a scholarship through the Netherlands Fellowship Programme (NFP) that enabled me to realize my dream.

Above all, my humble thanks goes to God Almighty for his grace and love that has taken me this far.

Table of Contents

List of Tables

LIST OF FIGURES

Abbreviations

ACT	Atmospheric Correction Tool
ASTER	Advanced Space borne Thermal Emission and Reflection Radiometer
BEAM	Basic ENVISAT Toolbox for (A)ATSR and MERIS
BRDFs	Bi-directional Radiance and Distribution Functions
CZCS	Coastal Zone Color Scanner
DN	Digital number
EOS	Earth Observing System
ESA	European Space Agency
ETM+	Enhanced Thematic Mapper Plus
FLAASH	Fast Line-of-sight Atmospheric Analysis of Spectral Hypercubes
FOV	Field of view
GCS	Geographic coordinate systems
GloVis	Global visualization viewer
GPS	Global position system
ISAC	In-Scene Atmospheric Correction
LST	Land surface temperature
MERIS	MEdium Resolution Imaging Spectrometer
MNF	Minimum noise fraction transformation
MODIS	Moderate Resolution Imaging Spectroradiometer
MODTRAN	Moderate Resolution Transmittance
MPB	Microphytobenthic
NASA	National Aeronautics and Space Administration
NCEP	National Centers for Environmental Predictions
NDVI	Normalised difference vegetation index
NIR	Near-infrared
OCTS (ADEOS)	Ocean Color and Temperature Scanner (Advanced earth observation satellite)
PPI	Pure pixel index
SAM	Spectral Angle Mapper
SeaWiFS	Sea-viewing Wide Field-of-view Sensor
SMAC	Simplified Method for Atmospheric Correction
SWIR	Shortwave infrared
TIR	Thermal Infra-red
TM	Thematic Mapper
UNEP	United Nations environmental programme
UNESCO	United Nations Educational, Scientific and Cultural Organisation
USGS	United States geological Surveys
UTC	Coordinated Universal Time
VNIR	Visible and near Infra-Red

List of Symbols

Symbol	Description	Units
Chl-*a*	Chlorophyll a concentration	$mg.m^{-2}$
E_0	Light intensity	$\mu mol\ m^{-2}\ s^{-1}$
Kd	Diffuse attenuation coefficient	mm^{-1}
L_d	Dowelling irradiance	$Wm^{-2}\ nm^{-1}$
L_u	Upwelling radiance	$Wm^{-2}\ sr^{-1}nm^{-1}$
PAR	Photosynthetically Available Radiation	Einstein $^{-2}d^{-1}$
P^B_{max}	Maximum rate of photosynthesis	mg C mg chl $a^{-1}\ h^{-1}$
R^2	Correlation coefficient	
Rrs	Remote sensing reflectance	sr^{-1}
Z	Euphotic depth	mm
α^B	Photosynthetic efficiency	mg C $chla^{-1}(\mu mol\ m^{-2}\ s^{-1})^{-1}\ h^{-1})$
σ	Standard deviation	

1. Introduction

1.1. Background

Intertidal mudflats are coastal wetlands that result from prolonged and consistent deposition of nutrient-rich estuarine silts, clays, or sand particles, and marine animal detritus by sea tides and rivers in shallow areas or within the intertidal zone (Adam *et al.*, 2009; Reise *et al.*, 2010; Stal, 2010). In this thesis, the intertidal zone refers to an area directly above water at low tide and below water at high tide. In the Wadden Sea a tidal cycle of inundation and exposure takes approximately 6 hours. Intertidal sediments are a habitat to pelagic and benthic microorganisms. These microorganisms are the major primary producers in intertidal mudflats and their presence enhances sediment stability through secretion of extracellular polymeric substances (Stal, 2010). Currently, the existence of intertidal mudflats is threatened by sea level rise, fragmentation, physical human development, dredging due to regular shipping activities, and changes in sedimentation patterns (CPSL, 2005; Reise. *et al.*, 2010).

Primary productivity refers to the chemical synthesis of organic compounds by autotrophs from inorganic carbon and nutrients (Abercrombie *et al.*, 1973). Intertidal mudflats primary productivity is generally high although spatially and temporally variable. This variability can be explained by the presence of different sediment morphological structures or characteristics and other related environmental variables. The variables include, diurnal temperature changes, seasonal patterns, nutrient availability, amount of incident light and concentration of diatoms within sediments (Brotas *et al.*, 1995; van der Wal. *et al.*, 2010). So far research has shown that intertidal mudflats primary productivity is largely dominated by pelagic and benthic micro algae and benthic micro fauna (Reise*, et al.*, 2010). Kromkamp *et al.,* (2006) has further stated that mudflats are currently classified as the most productive ecosystems in the world because of benthic algae primary productivity. These microorganisms form the basis of the food web that ultimately provides food and enrich aquatic nursery (Reise*, et al.*, 2010). However, despite their ecological significance, the knowledge of primary productivity of benthic micro fauna and benthic microalgae in intertidal mudflats is limited. Understanding microphytobenthic primary productivity in intertidal mudflats is necessary for ecosystem modelling, prediction and management. In this regard, it is important to find ways of estimating the spatial and temporal variations of microphytobenthic primary productivity in intertidal mudflats.

Microphytobenthic (MPB) organisms are a composition of benthic single-celled phototrophic microorganisms or microalgae forming biofilms on intertidal sediment surfaces (Paterson *et al.,* 2001). The existence of MPB in intertidal environments is bio-physically and ecologically crucial. This can be seen through their different roles in determining the functioning of the intertidal ecosystem (fig. 1-2). They stabilize estuarine sediments from re-suspension during high tidal periods, through the excretion of extracellular polymeric substances that glue sediment grains together (Adam*, et al.*, 2009; Blanchard, 2000; Kromkamp *et al.*, 2006). MPB are the most important phototrophic microorganisms in intertidal mudflats ecosystem, constituting the bulk of estuarine total primary productivity (Barranguet. *et al.*, 2000; Blanchard, 2000; Underwood *et al.*, 1999). The distribution of these organisms in intertidal mudflats is heterogeneous, as they vary spatially with the observed variation in the nature of sediment types within the Wadden Sea area as a function of an inter-play of different prevailing environmental factors. Thus, to better understand primary productivity in these areas; deriving information on different sediment classes is one of the critical steps. It is argued that over sandy silts and sands the concentrations of MPB biomass is very low as compared with areas of fine cohesive clay sediments (Sundback *et al.*, 1991). Sands tend to be both lower in nutrients and frequently resuspended than cohesive sediments, and these characteristics probably contribute towards lower MPB biomass (fig 1-2). In addition, the estimation of areas of active MPB primary productivity as well as understanding the role of MPB in estuarine environments is important as this can assists in managing estuarine critical environment. The patterns of MPB primary productivity in intertidal mudflats are heterogeneous both spatially and temporally but to the best of our knowledge this variability is poorly understood. Areas of active primary productivity in intertidal mudflats in the Wadden Sea are not known. This limitation has been attributed to the very patchy nature of their occurrence. Again, this problem is further explained by the short term dynamic nature of MPB biomass availability in the euphotic zone within the sediment profile, caused by the vertical migration of epipelic diatoms from time to time (Barranguet*., et al.*, 2000; Kromkamp*, et al.*, 2006).

Figure 1-1: Intertidal mudflat areas where benthic microorganisms result in MPB primary productivity

Traditionally, intertidal mudflat primary productivity has been derived through sediment coring techniques followed by laboratory MPB biomass analysis. However, this method is cumbersome and requires intense and prolonged field measurements which is time consuming, challenging and costly. In addition, a close analysis of the findings from these traditional methods indicates that they are limited to micro-scales whereas remote sensing techniques provide an opportunity to a wide spatial coverage at a given time. The advent of high resolution remote sensing data offers a better alternative means of obtaining essential information to study intertidal mudflats (Adam*, et al.*, 2009; DerondeKempeneers *et al.*, 2006; Murphy *et al.*, 2008; van der Wal *et al.*, 2004). Satellite remote sensing data has the capability of providing a consistent and full spatio-temporal coverage of intertidal mudflat areas. The technique also provides non-intrusive measurements of areas considered to be inaccessible and highly sensitive to any physical disturbances such as trampling (Adam*, et al.*, 2009). Remote sensing and GIS techniques enhances spatio-temporal investigations of ecological and physical environments by providing synoptic images of intertidal areas at minimal costs (van der Wal*., et al.*, 2010). In this regard this study explores the possibility of using remote sensing techniques and ground based measurements in estimating and mapping microphytobenthic primary productivity in intertidal mudflat sediments of the Wadden Sea.

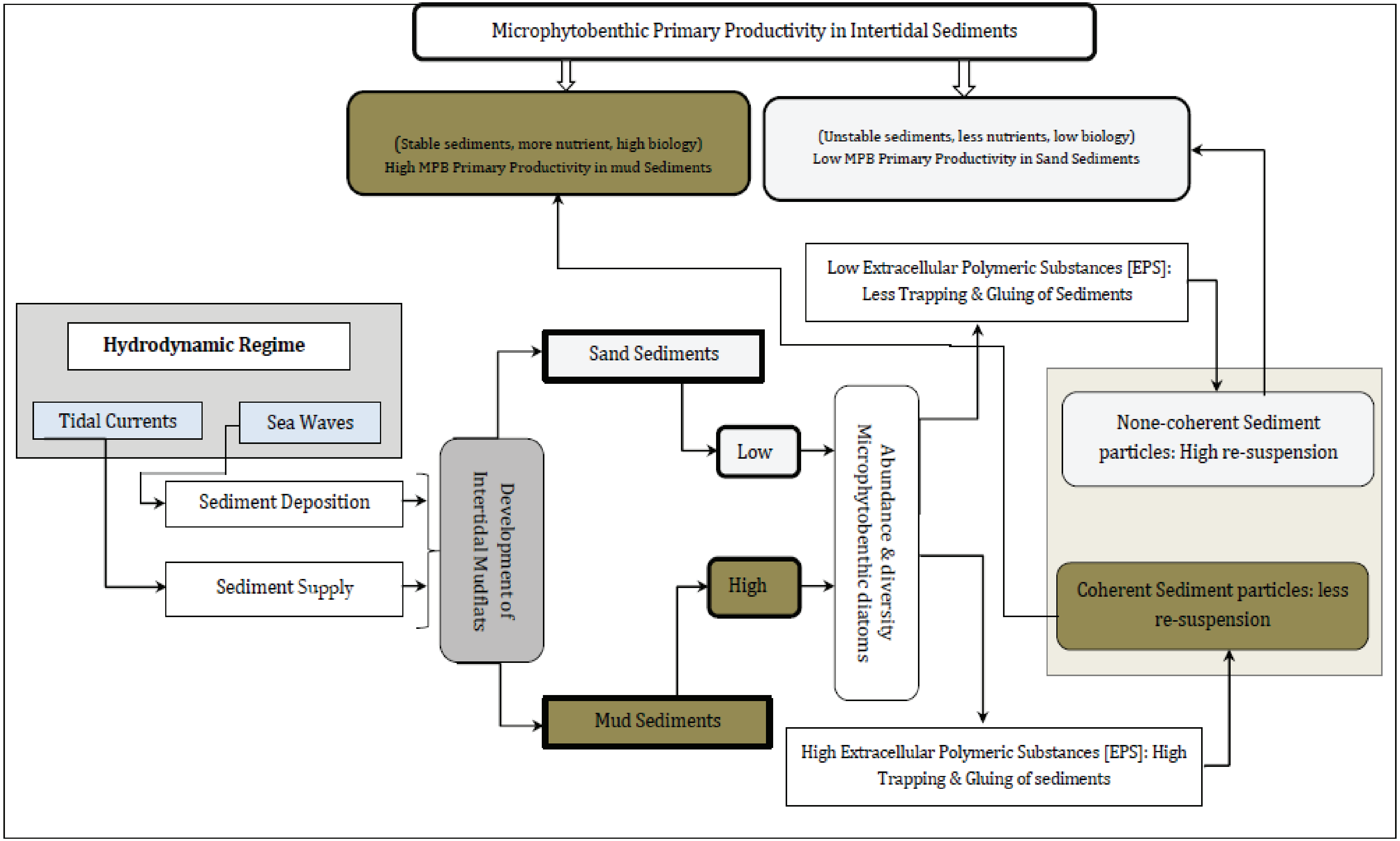

Figure 1-2: Modified Conceptual framework illustrating the interactions between biology, hydrodynamics and sediments in intertidal mudflats adapted from Stal, (2010). From the conceptual framework this study concentrated much on the areas highlighted in bold.

1.2. Research Problem

Despite MPB primary productivity in intertidal sediment surfaces having an undisputable ecological role, methods of its quantification have proven to be difficult (Jesus *et al.*, 2006) and cumbersome hence posing problems in monitoring and coming up with possible management strategies. Currently, the knowledge on MPB primary productivity in intertidal mudflats of the Dutch Wadden Sea is rudimentary. This limitation is attributed to factors such as: (i) the sparse nature of in-situ data in both time and space over the area as a result of area inaccessibility (Jesus*, et al.*, 2006) and the patchy nature of their occurrence that is determined by variations in the texture and relief of the sediments surface (Adam*, et al.*, 2009; Jesus*, et al.*, 2006; Kromkamp*, et al.*, 2006; Smith *et al.*, 2004). (ii) Quantification of chl-*a* concentrations, which is a proxy of benthic biomass, on intertidal mudflats using traditional sampling techniques is more challenging (Kromkamp*, et al.*, 2006), tedious, expensive, labour-intensive, ecological destructive and does not fully capture the spatial heterogeneity since measurements are done on a point basis Adam, De Backer *et al.* (2011). (iii) Chl-*a* content in mudflats is normally limited in amount. (iv) MPB primary productivity rates change rapidly within a short period of time (Barranguet.*, et al.*, 2000). These factors have resulted in limited understanding of MPB biomass and productivity. Consequently, methods that will capture the spatial and temporal variations of MPB such remote sensing provide a platform for understanding MPB primary productivity. The inherent intertidal mudflats sediment characteristics and chl-*a* optical properties allow remote sensing of MPB primary productivity in these delicate areas (Jesus*, et al.*, 2006).Thus this research attempts to bridge this gap by coupling in-situ and with remote sensing data to estimate MPB primary productivity and map its variability in intertidal sediment surfaces. (Jesus*, et al.*, 2006).

1.3. General Objective

To estimate microphytobenthic primary productivity from the exposed intertidal mudflats using remote sensing in the Dutch Wadden Sea, The Netherlands

1.4. Specific Objectives

1. To derive information on the characteristics of the top sediment layer of mudflats in the Dutch Wadden Sea using field and remote data,
2. To estimate chl-*a* content from intertidal mudflats using NDVI as a proxy for biomass,
3. To derive maps of MPB primary productivity from intertidal mudflats in the Wadden Sea.

1.5. Tasks

- To determine different sediment spectral characteristics,
- To map the spatial variation of MPB using Spectral Angular Mapper algorithm,
- To derive land surface temperature from remote sensing data,
- To determine intertidal areas rich in microphytobenthic biomass and active primary producers, and
- To produce maps of MPB primary productivity of intertidal mudflats of the Wadden Sea.

1.6. Research Questions

1. How does spectral reflectance vary with sediment type?
2. Does chl-*a* content or NDVI vary significantly with spatially variations in sediment properties?
3. What is the MPB primary productivity of the Wadden Sea?

1.7. Research Findings

- To produce intertidal sediment ecotopy maps,
- Derive chl-*a*+ phaeo pigments spatial distribution maps over the Wadden Sea area,
- Map land surface temperature maps from ASTER and Landsat (TM and ETM+) thermal bands,
- Compute a linear relationship between P^B_{max} and temperature,
- Intertidal mudflat primary productivity maps of the Dutch Wadden Sea,
- Sensitivity analysis results of MPB primary productivity on intertidal mudflats.

1.8. Thesis Structure

For simplicity, each objective in this study has been treated as a separate chapter, with each method accompanied by the respective results and discussions. The whole thesis document consists of nine chapters. Chapter 1 comprises of the introduction which gives a comprehensive overview of the research including problem statement, objectives, research questions, research outputs, and innovativeness of the study. Chapter 2 outlines the general description of the study area. Chapter 3 consists of data and materials used in this study. Chapter 4 is a detailed outline of data pre-processing steps: calibration and atmospheric of remote sensing data. Chapter 5 entails the detailed approach adopted to derive information intertidal sediment types and the results are discussed in chapter 6. Chapter 7 is about methods used to estimate MPB primary productivity from the Wadden, whereas chapter 8 outlines an in depth results and discussion from chapter 7. Conclusions and recommendations are summarised in chapter 9. Figure 1-3 outlines the general thesis conceptual matrix.

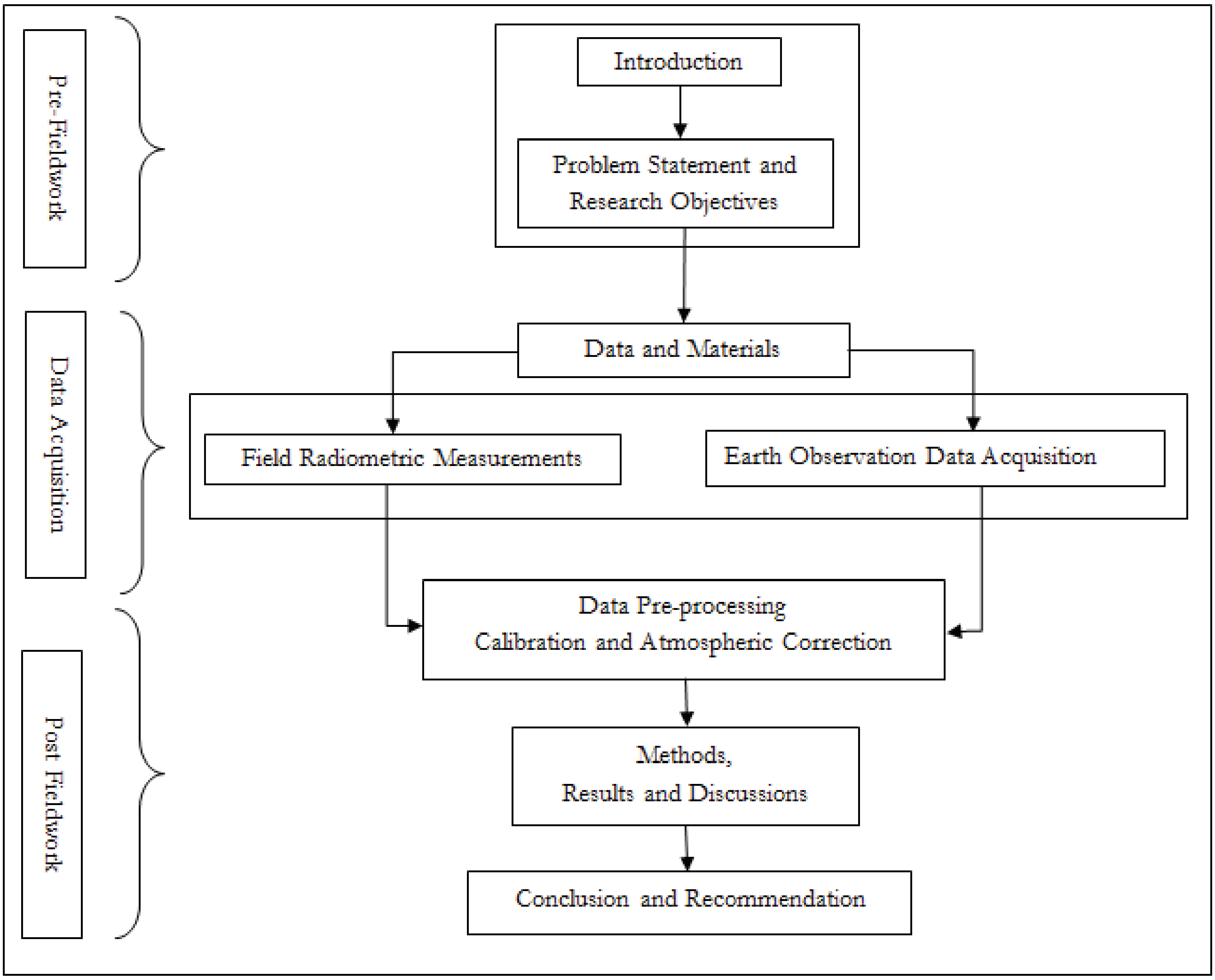

Figure 1-3: Thesis matrix

2. Description of the Study Area

2.1. Geographic Location of the Wadden Sea

The Wadden Sea is by nature a shallow open intertidal region with estuarine character (CPSL, 2005). It covers a wide land area with an aerial coverage of approximately 10 000km² in total and about 500 km in length (Hogan, 2011; Hommersoms, 2010). The area is located in the SE part of the North Sea on latitude 52°52'N to 53°33'N and Longitude 04°45'E to 07°13'E (UNEP, 2009). It stretches from Den Helder Netherlands where it is flanked from Ijsselmeer by the Afsluitdijk in the south west, through the great river estuaries of Germany to its northern frontier at Skallingen north of Esbjerg in Denmark (Hogan, 2011; Hommersoms, 2010; Otto *et al.*, 2001). The area is internationally recognized as one of the World's largest natural landscape that remains in Europe, with a high ecological, economic and societal significance (Otto*, et al.*, 2001). Most of the natural processes in this area continue to function undisturbed. In June 2009 the Wadden Sea was included to the World Heritage list by UNESCO (Hommersoms, 2010; UNEP, 2009). Its ecological significance is mostly centred on biological diversity that is based on coastal habitats such as mudflats, sea grass beds, salt marshes, mussel beds, and estuaries (Reise*, et al.*, 2010).

According to Otto and Zuidbroek, (2001), the area is well-known for its biological diversity and high productivity sustaining large populations of shorebirds, ducks, and geese. Some of the bird species use the area as a flying stop zone (Karsten et al., 2009). The major habitats and land cover types are salt marshes; covered with *halophilous* vegetation with sand dunes and tidal flats that provide a home to micro and macro algae (Reise.*, et al.*, 2010). Eutrophication supplies the Wadden Sea with an overabundance of algae (Hommersoms, 2010; Reise.*, et al.*, 2010; UNEP, 2009). Together with suspended matter, the algae make the water too turbid for seaweed to develop well. In addition, the gradual encroachment by embankment of the adjoining salt-marshes and coastal embayment is causing the Wadden Sea to shrinks in size (Reise*, et al.*, 2010). Research and monitoring is necessary to increase our understanding of the system to be able to reduce further environmental degradation.

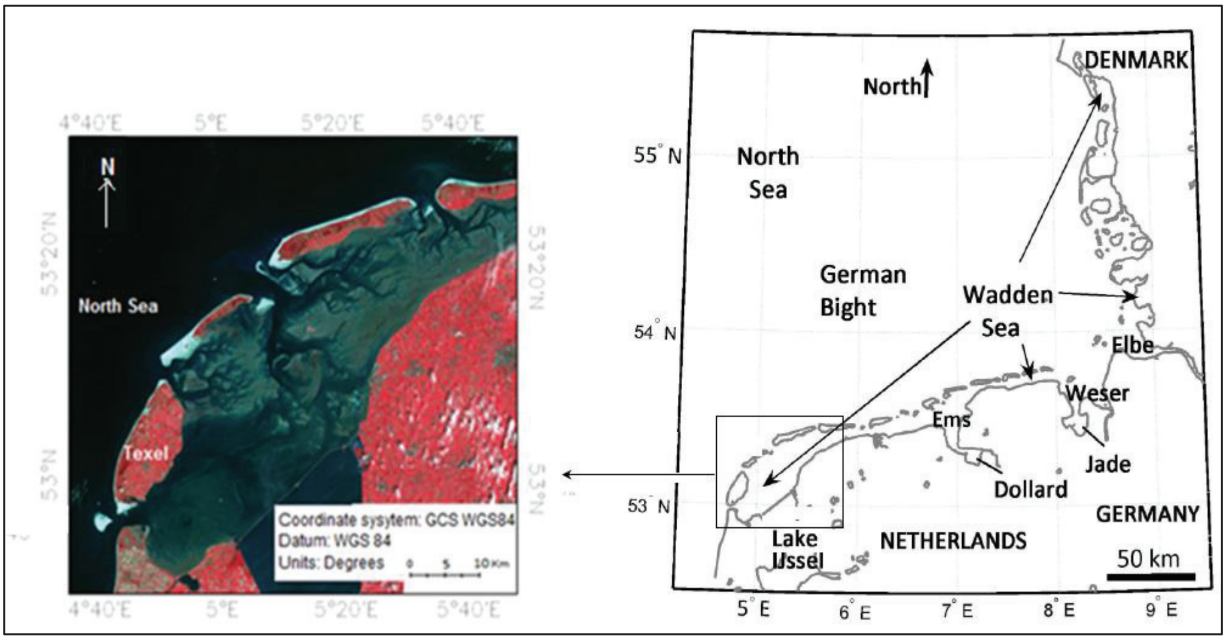

Figure 2-1: False- colour composite map of the Wadden Sea with special reference to the Dutch part (Source: Aster 2007) and adapted from Hommersoms (2010).

2.2. Climate

The Wadden Sea experiences temperate climatic conditions. Its climatic conditions are defined by the convergence of two different air masses. These include the humid maritime air mass coming from the west and the dry continental air mass originating from the east. These air masses results in mild winters and cooler summers over the Wadden Sea (UNEP, 2009). Even though the prevailing climatic conditions of the area are characterised by cooler periods, generally there are often more sun hours per annum in these coastal regions.

Table 2-1: Mean temperatures over the Wadden Sea

Mean temperatures	Temperatures [^{0}C]
Mean annual air temperature	8.5
Mean annual water temperature	9
Summer mean	15
Winter mean	4

Temperatures of the area are as indicated in table 2.1. For the past six decades (1950 to 2010) the extreme water temperatures were ±2.3°C in the tidal region (UNEP, 2009). Although the sea is the source of humid air, precipitation in the Wadden Sea area is moderate, ranging from 700 to 800 mm yr^{-1} or approximately 2 mm d^{-1} (UNEP, 2009).

2.3. Topography

The Wadden Sea landscape is made up of flat coastal plains and the lowly-elevated offshore barrier islands with an altitude of approximately ± 50m above sea level. Coastal sand dunes, beach ridges and dykes constitute the main topographic types in the area (UNEP, 2009). These physical features have a significant role in protecting low-lying freshwater marshes and agricultural fields from the rage of environmental disasters like flooding.

2.4. Biodiversity and Conservation

Wadden Sea is characterised by endemic species. The endemic species make the Wadden Sea a unique biotype when compared to other global biomes (Reise*, et al.*, 2010). A report by UNEP, (2009) has indicated that approximately 2 300 flora species and 4 200 fauna species survive from the rich spectrum of distinct microhabitats are found in this area. So far, the terrestrial vegetation of the Wadden Sea is predominantly characterized by the highest species diversity that is linked to salt marshes (UNEP, 2009). According to Reise, *et al.,* (2010) the area is home to about 6 million birds yearly. So far, the natural intertidal environments make the area to be recognised as a highly productive ecosystem in the world. For example, research has shown that, the area provides home to an estimate of 10,000 species of unicellular organisms, plants, fungi and animals(UNEP, 2009).

2.5. Economic Function

Economically, the Wadden Sea ecosystem acts as the hub for commercial fisheries in the North Sea due to the fact that it ecological functions as a staging area for fish migrating between rivers for spawning and the oceans for feeding (Reise*, et al.*, 2010). According to Hofstede *et al.,* (2005) statistics indicate that around 10 million tourists and 30-40 million daily visitors come to the Wadden Sea area every year, raising approximately 1.5 billion Euro to the total tourism earnings annually (IRWC, 2000a).

3. Data and Materials

This chapter presents a brief description of the instruments, field measurements methods and remote sensing datasets used in the study.

3.1. Pre-fieldwork

Pre-fieldwork was characterized by acquisition of radiometric instruments such as TriOs- RAMSES irradiance and radiance sensors (fig 3-1). These instruments were calibrated and tested to see whether they were functional before leaving for fieldwork. Selected instruments and materials are listed in section 3.1.1 below.

3.1.1. Fieldwork materials and Instruments

Figure 3-1: TriOs RAMSES Irradiance and Radiance sensors[1]

The following fieldwork equipments and materials were supplied by ITC.

- Garmin etrex Global Position System (GPS)
- Navigation compass and 1 m tripod,
- Aluminium trunk for storing fieldwork materials
- TriOs RAMSES irradiance and radiance sensors
- Water proofed gumboots
- Notebook (laptop)

3.2. Field Radiometric Measurements

3.2.1. Field Endmember Spectra Collection

In-situ field radiometric measurements were conducted as part and under the IN PLACE activities on exposed intertidal mudflat sediment surfaces between the 26th and 28th of September 2011 in the Wadden Sea, the Netherlands (fig 3-3). The field surveys were conducted based on predicted tidal cycle (fig 3-2). The first two days were covered by clouds whereas the last day was clear and sunny. The measurements were conducted following the IN PLACE measurement protocol as briefed hereafter (Personal communication with Salama 2011). The TriOs RAMSES with the ACC-VIS irradiance sensor and radiance sensor were used to measure upwelling radiance ($Wm^{-2}\ sr^{-1}\ nm^{-1}$) and downwelling irradiance ($Wm^{-2}\ nm^{-1}$). These measurements were specifically done on undisturbed sediments surfaces so as to capture an undistorted distribution of microphytobenthic diatoms in mudflats. Downwelling irradiance $E_d(0^+, \lambda)$ was measured at an angle of 135^0 while on the other hand, upwelling radiance $L_u(0^+, \lambda)$ with a field of view of 7^0 and an angle of 40^0. All these measurements were done simultaneously from a fixed height of

[1] http://www.trios.de/index.php?option=com_content&view=category&layout=trios&id=47&Itemid=76&lang=en#item196_top

110 cm above the intertidal surface sediments so as to increase the radiometric footprint. Spectral signature values were assessed for consistence through plotting spectral graphs against wavelength in the field after taking some measurements. Assessment was conducted with the help of an expert (Salama). When unsatisfied with the results, adjustments were made until satisfactory measurements were attained.

Since in the Wadden Sea a tidal cycle of inundation and exposure takes approximately 6 hours per day, radiometric measurements were done following the predicted tidal tables from 12:40 to 17:00pm (UTC). During this low-tide period, the intertidal mudflats were exposed enabling sampling (fig 3-2). Three sites were chosen for radiometric measurements. From each site, radiometric measurements were taken on different days (table 3-1). The coordinates of the sampling sites were recorded using a Garmin etrex global position system (GPS). A total of 37 locations were measured from three sites. Three different sites were chosen for radiometric measurements because microphytobenthic presence on Wadden Sea intertidal mudflats varied from one place to another as a function of the existing different sediment types.

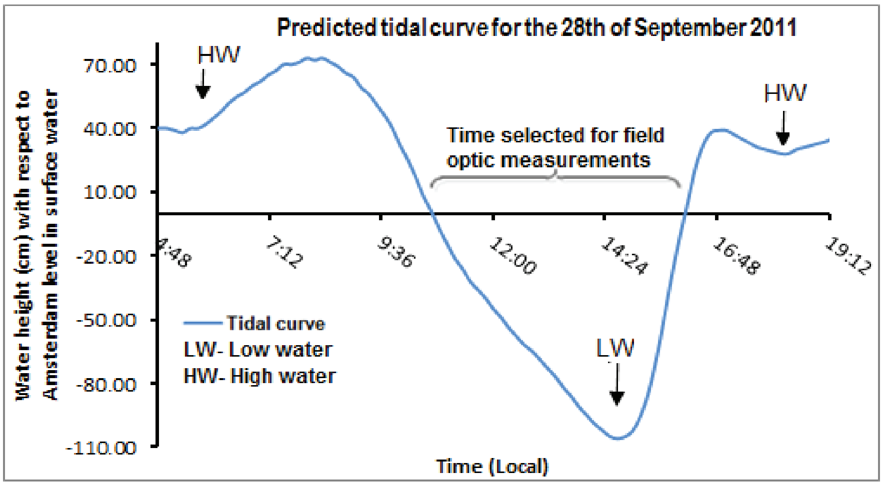

Figure 3-2: Schematic illustration of the predicted tidal cycle for the 28th day of September 2011 that was used to undertake radiometric measurements in intertidal mudflats.

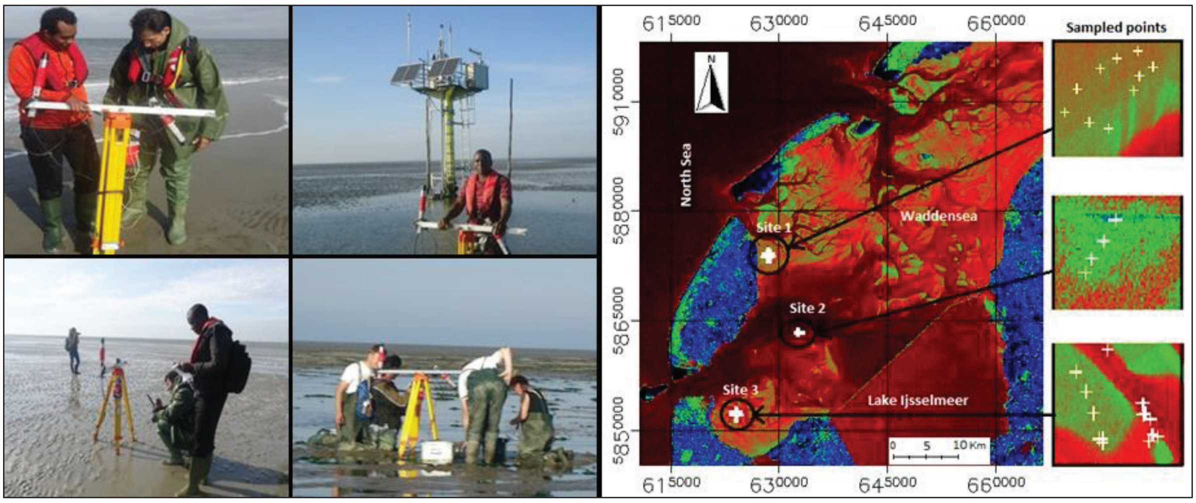

Figure 3-3: Field instrument measurement setup and field sampled sites

Table 3-1: Coordinates of the intertidal mudflat sites sampled at low- tide

Date	Station	Lat N	Long E	Location	Vessel	Sample Points
26.09.2011	Site 1	53°2.460	04°58.426	Lutjeswaard	Zeevonk	6
27.09.2011	Site 2	53°4.193	04°53.181	Vlakte van Kerken	Zeevonk	13
28.09.2011	Site 3	52°57.225	04°50.213	Balgzand	Zeevonk	18
29.09.2011	Reserved for bad weather					

3.3. Earth Observation Data Acquisition

3.3.1. Landsat (ETM and TM), Aster and Meris Images

Three Landsat images, two Aster and one Meris day time images were used. Landsat images were acquired from the ready available online Landsat archive. The archive was accessed via the US Geological Survey Global Visualization Viewer (GloVis) through http://glovis.usgs.gov/ web-link. Aster level 1B images were acquired via the ITC RSG lab, whereas Meris images were acquired from ESA. During the acquisition process, images were selected based on the following criteria: (i) they should be acquired during a period of low tidal (ii) they must be free of cloud cover. Based on these criteria, only a few images were found to be suitable for deriving information on sediment types (table 3-3). To confirm whether the images were collected during a period of low tide we retrieved information on tidal water height from an online tidal database[2]. Den Helder which is in the Western part of Wadden Sea was used as the reference. The water heights were presented in centimeters (cm) based on normal Amsterdam surface level (fig 3-4). The spatial and temporal resolution of the selected remote sensing datasets is summarised in table 3-2 below.

Table 3-2: Descriptive information of acquired earth observation data

Satellites	Characteristics		
	Spectral Resolution	**Spatial Resolution**	**Orbital**
Meris	VIS-NIR (15bands) Across range 390nm-1040nm	Ocean 1040m*1200m (Reduced Resolution). Coastal 260m*300m Full Resolution.	Polar orbital. Sun synchronous. FOV 68.5deg. Swath width 1150km. 3 day overpass time
Landsat (TM and ETM)	0.45μm - 12.5μm. (7 bands) (VIS,NIR,MIR)	30m*30m :- (VIS, NIR, MIR). 60m*60m:-thermal.	Near polar orbital. Sun synchronous, Inclination 8.2deg. 16 days (233 orbits). Altitude 705km
Aster	14 bands, VIS-NIR(1-3), SWIR (4-9), TIR (10-14)	VIS_NIR 15m SWIR 30m TIR 90m	Near polar orbital. Sun synchronous, Orbital inclination 98.3° from equator. Altitude 705km. 16 day repeat cycle

[2] http://live.waterbase.nl/waterbase_wns.cfm?taal=nl

Table 3-3: Landsat scene data acquisition information

Data Description	Date Acquired	Lat	Lon	Path	Row	Spatial Resolution	Max Cloud
Landsat ETM+	2000/05/13	53.1	5.7	198	23	30 m	0.0 %
Landsat TM 5	2009/07/01	53.1	5.7	198	23	30 m	18 %
Landsat TM 5	2010/09/06	53.1	5.7	198	23	30 m	0.0 %
Aster	2003/10/05	53.1	5.7	198	23	15 m	-
Aster	2007/05/07	53.1	5.7	198	23	15 m	-
Meris	2011/09/28	53.1	5.7	-	-	300m	-

(Source: http://glovis.usgs.gov/)

3.4. Wadden Sea tidal Water Heights

The figure below illustrates six different tidal cycles corresponding to specific dates in which above mentioned remote sensing images were acquired. From all the images it is observed that on each day there is more than four hours of intertidal exposure from sea tides.

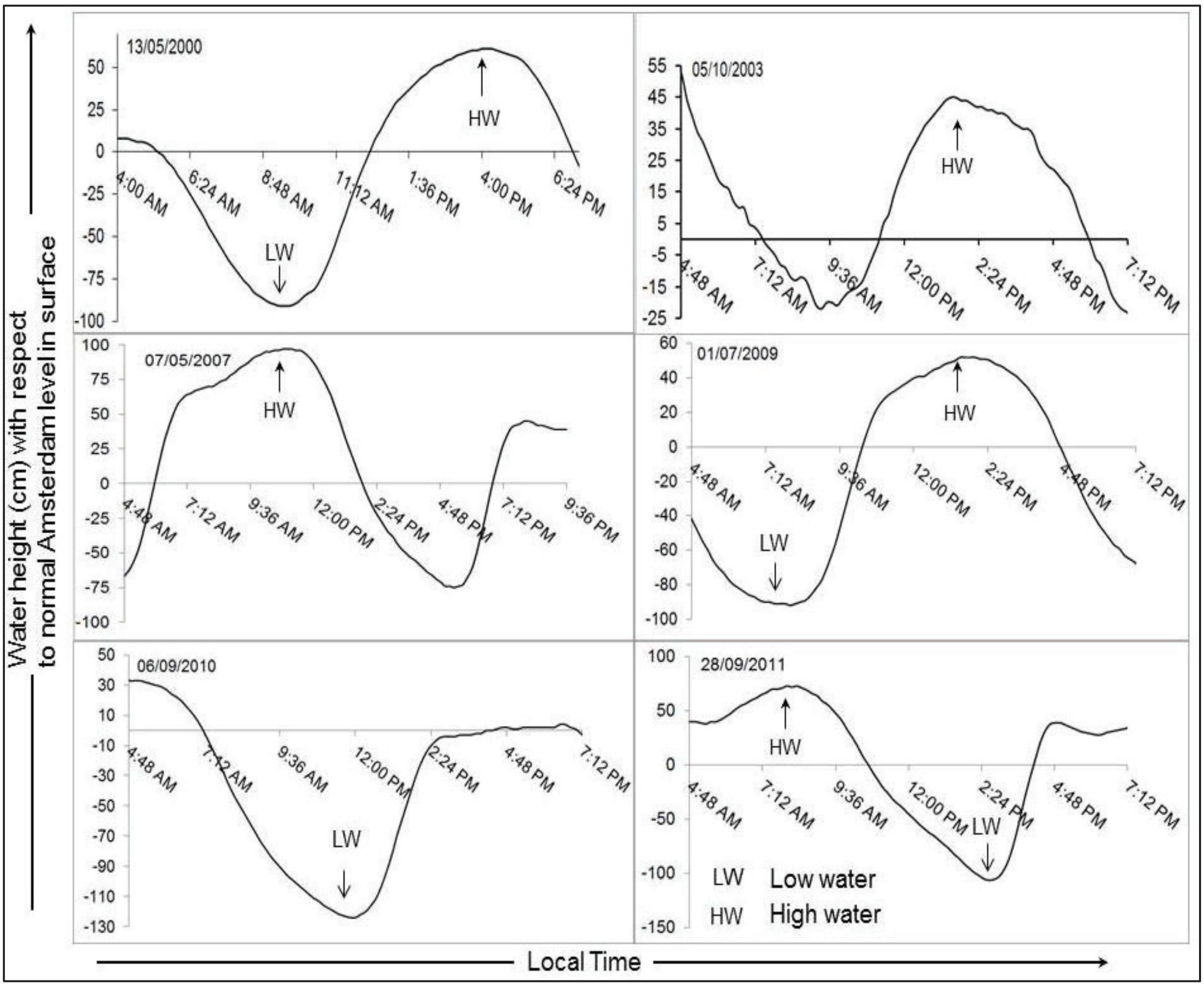

Figure 3-4: Predicted tidal water heights in centimetres (cm) for the Wadden Sea in relation to selected dates in which images where acquired for analysis.

4. Data Preprocessing

4.1. Field Data

Downwelling irradiance and upwelling radiance derived from the TriOs RAMSES sensors were used to derive the remote sensing reflectance for different sediment types. Remote sensing reflectance was determined directly by computing the ratio of upwelling radiance and downwelling irradiance as shown in equation 4.1 below.

$$Rrs = \frac{L_u(0^+,\lambda)}{E_d(0^+,\lambda)}, \qquad [sr^{-1}] \tag{4. 1}$$

Where

Rrs = remote sensing reflectance [sr^{-1}],

L_u $(0^+, \lambda)$ = upwelling radiance [Wm^{-2} sr^{-1} nm^{-1}],

E_d $(0^+, \lambda)$ = downwelling irradiance [Wm^{-2} nm^{-1}].

However, to derive information on sediment types from remote sensing data, remote sensing reflectance was converted to spectral reflectance by multiplying the resultant output by pi (π). Based on this method, three spectral endmember classes were determined from remote sensing data for ecotopy mapping (fig 4-1). These consist of sea weed (vegetation), clay and sand. In this study, a spectral endmember is defined as a specific pure spectral feature acquired through in-situ radiometric measurements or laboratory analysis of reflectance spectra; principally focusing on a single surface (Hommersoms, 2010; Schwengerdt, 1997; Yuhas *et al.*, 1992). According to De Carvalho *et al.,* (2000) this method is predominantly grounded on expert know-how of the landscape investigated.

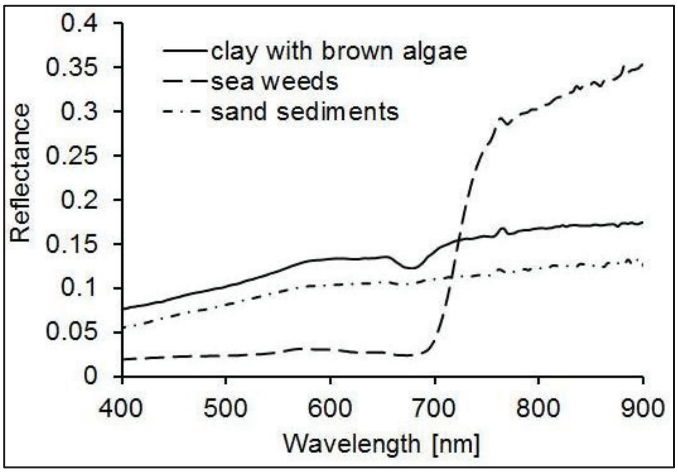

Figure 4-1: Spectral signature of different sediment types in intertidal mudflats, the Wadden Sea

4.2. Calibration of Earth Observation Data

4.2.1. Landsat (TM and ETM) Calibration

All Landsat images were acquired in Digital Number (DN) format. However, for these images to be used in deriving information on mudflats sediment types, they had to be first calibrated into spectral radiance units [$Wm^{-2}sr^{-1}\mu m^{-1}$] following the calibration method by Chander *et al.,* (2009). The calibration coefficients were provided together with the respective Landsat images as tabulated in table 4-1. The conversion from DN to spectral radiance was done band by band; through implementing the following mathematical formulation by Chander *et al.,* (2009) indicated below in equation 4.2:

$$L_\lambda = \left(\frac{LMAX_\lambda - LMIN_\lambda}{Q_{cal\max} - Q_{cal\min}} \right) (Q_{cal} - Q_{cal\min}) + LMIN_\lambda \tag{4. 2}$$

Where
L_λ = spectral radiance at the sensor's aperture [$Wm^{-2}sr^{-1}$ μm^{-1}],
Q_{cal} = Quantized calibrated pixel value [DN],
Q_{calmin} = Minimum quantized calibrated pixel value corresponding to $LMIN_\lambda$ [DN],
$Qcalmax$ = Minimum quantized calibrated pixel value corresponding to $LMAX_\lambda$ [DN],
$LMIN_\lambda$ = Spectral radiance that that is scaled to Q_{calmin} [$Wm^{-2}sr^{-1}$ μm^{-1}],
$LMAX_\lambda$ = Spectral radiance that that is scaled to Q_{calmax} [$Wm^{-2}sr^{-1}$ μm^{-1}],

Table 4-1: Landsat TM and ETM+ calibration coefficients

TM Sensors [Qcalmin=1 Qcalmax=255]				
Band	Spectral Range	Center wavelength	$LMIN_\lambda$	$LMAX_\lambda$
Units	µm		W/[m^2 sr µm]	
L5TM [LPGS]				
1	0.452-0.518	0.485	-1.52	193
2	0.528-0.609	0.569	-2.84	365
3	0.628-0.693	0.660	-1.17	264
4	0.776-0.904	0.840	-1.51	221
5	1.568-1.784	1.676	-0.37	31.4
7	2.097-2.347	2.223	-0.15	16.5

L7 ETM+ Sensors [Qcalmin=1 Qcalmax=255]				
Band	Spectral Range	Center wavelength	$LMIN_\lambda$	$LMAX_\lambda$
High gain [LPGS]	µm		W/[m^2 sr µm]	
1	0.452-0.514	0.483	-6.2	191.6
2	0.519-0.601	0.560	-6.4	196.5
3	0.631-0.692	0.662	-5.0	152.9
5	1.547-1.748	1.648	-1.0	31.06
7	2.097-2.349	2.206	-0.35	10.80
Low gain [LPGS]				
4	0.772-0.898	0.835	-5.1	241.1

4.2.2. Aster Calibration

Aster level 1B contains radiometrically calibrated and geometrically co-registered data (YCEO, 2011) with 6 SWIR, 3 VNIR and 5 TIR bands having different resolution (table 3.2) and a single band pointing backwards to generate a parallax information on elevation. This band was not included in classification. The satellite provides geo-spatial information on land surface temperature, digital elevation and surface reflectance. The Aster scene has nearly 60 km by 60 km aerial coverage. The sensor concurrently acquires geo-spatial data in three distinct spectral resolutions (http://asterweb.jpl.nasa.gov/).

4.2.3. Meris Calibration

Meris level 1B were used in this study and these images are readily geometrically calibrated so as to be matched with the Top-Of-Atmosphere (TOA) radiance[3].

4.3. Atmospheric Correction of the Visible and Thermal Channels

By nature satellite remote sensing data are affected by atmospheric effects such as atmospheric aerosol scattering as well as non-target effects from the earth's surface due to adjacent effects. This is attributed to the fact that the incoming solar radiation has to pass through the atmosphere before it is measured by

[3] http://envisat.esa.int/handbooks/meris/CNTR2.htm

remote sensing instruments as illustrated in figure 4-2 (Azab, 2012; Trishchenko *et al.*, 2002). Therefore, for improved quantitative analysis of surface reflectance, there is need to critically perform atmospheric correction to get rid of non-target effects, thus, enhancing surface reflectivity properties (Azab, 2012; Fallah-Adl *et al.*, 1995; Trishchenko*, et al.*, 2002).

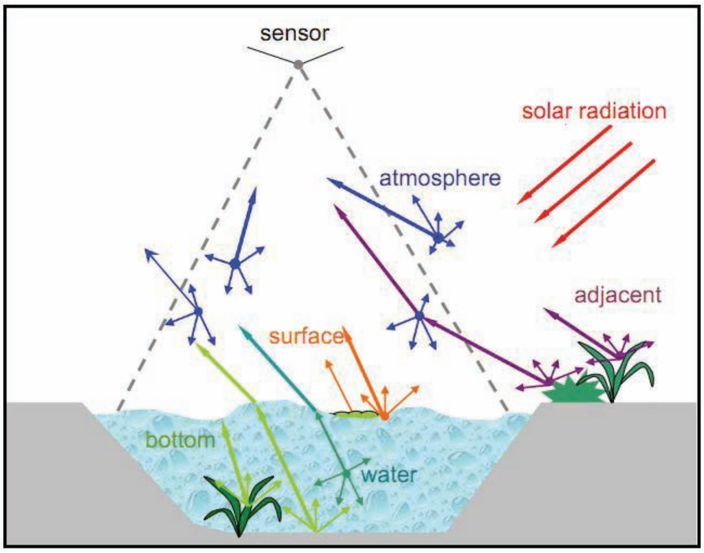

Figure 4-2: Schematic illustration of remote sensing technique.

4.3.1. Visible Bands Atmospheric Correction

The visible bands for Landsat (TM and ETM+)and Aster images were atmospherically corrected using the FLAASH model (eq 4.3) (Felde *et al.*, 2003; Kaufmann *et al.*, 1997). The FLAASH model is only applicable to 0.35 μm- 2.5 μm visible region of the electromagnetic wavelength. It is one of the best atmospheric correction methods for retrieving reflectance from multispectral radiance images (Kaufmann*, et al.*, 1997; Trishchenko*, et al.*, 2002). On the other hand, Meris was corrected for atmospheric effects using SMAC which is a semi- empirical approximation of the radiative transfer in the atmosphere (Rahman *et al.*, 1994). Both models incorporates the MODTRAN4 radiation transfer code (Berk, 2000). The MODTRAN-4 code involves the application of a correlated-k algorithm which significantly enables precise computation of various scattering[4]. Actually, more accurate computations of transmittance and radiance enable an improved anaylsis of multispectral data. More so, the MODTRAN code also provides a set of Bi-directional Radiance and Distribution Functions (BRDFs) which permit ground scattering to be computed instead of being Lambertian. BRDFs and correlated-k algorithms are crucial in enhancing the scattering accuracy, since it includes the azimuthal asymmetries[5]. Spectral radiances were computed as illustrated in equation 4.3:

$$L = \left[\frac{A\rho}{1-\rho_e S}\right] + \left[\frac{B\rho_e}{1-\rho_e S}\right] + L_a \qquad (4.\ 3)$$

Where:

[4] [4] http://www.kirtland.af.mil/library/factsheets/factsheet.asp?id=7915
[5] http://www.kirtland.af.mil/library/factsheets/factsheet.asp?id=7915

ρ = the pixel surface reflectance,

ρ_e = the average surface reflectance for the pixel and the surrounding area,

S = the spherical albedo,

L_a = the radiance back scattered by the atmosphere [Wm^{-2} sr^{-1} nm^{-1}].

A and *B* are the transmittance coefficients that depend on atmospheric and geometric conditions but not on the surface.

All the above stated parameters depend on the spectral channel. *L* in equation 4.3 is equal to radiance reflected from the surface, directly detected by the sensor while the 2nd component corresponds to radiance from the ground which is scattered by the atmosphere into the sensor. The difference between r and re accounts for the adjacent influence instigated by the atmospheric scattering (Kaufmann*, et al.*, 1997). Following this method, correction of adjacent effect is neglected by assuming re=r.

The difference between ρ and ρ_e account for adjacent effect. *A, B, S* and L_a are directly derived from MOTRAN4 computations based on satellite viewing angle, solar angles and the average surface elevation (Kaufmann*, et al.*, 1997). *A, B, S* and L_a values are largely dependent on the water vapour column amount and which is normally unknown. Therefore, to account for this drawback, the MODTRAN4 computations are integrated over a sequence of various column amounts, and then selected image bands are investigated to derive an estimated amount for each pixel (Azab, 2012; Kaufmann*, et al.*, 1997). Radiance averages are derived for two set channels: an absorption set centred at the water band and a reference set of bands taken out of the channel. Following this step, a look-up table is generated for retrieving water vapour from the above generated radiances. When water vapour is retrieved, equation 4.3 is calculated for the pixel ground reflectances in all input image channels (Azab, 2012). The resultant method includes calculating a spatially averaged radiance image *Le*, while from the spatially averaged reflectance *re* is estimated using the formula below:

$$L_e = \left(\frac{(A+B)\rho_e}{1-\rho_e S} \right) + L_a, \tag{4.4}$$

4.3.2. Thermal Atmospheric Correction

Landsat (TM and ETM+) thermal bands were calibrated based on the same method by Chander *et al.,* (2009) as illustrated in equation 4.2. In order to retrieve accurate land surface temperature, these bands were atmospherically corrected for atmospheric effects (fig 4-2). According to Barsi, (2007), atmospheric correction is actually a pre-requisite for thermal imagery because upwelling emitted ground signal is usually attenuated and/or enhanced by the atmosphere. Then, brightness temperature was derived by following the approximation method of Goetz (1995) below:

$$T_b = \frac{k_1}{\ln\left(\frac{k_2}{B_6(T_6)} + 1 \right)} \tag{4.5}$$

Where

T_b = brightness temperature,

k_1 and k_2 = pre-launch calibration constants (607.76 $Wm^{-2}sr^{-1}\mu m^{-1}$ for L5, 666.09 $Wm^{-2}sr^{-1}\mu m^{-1}$ for L7 and k_2 =1260.56 $Wm^{-2}sr^{-1}\mu m^{-1}$ for L5, 1282.71 $Wm^{-2}sr^{-1}\mu m^{-1}$ for L7),

$B_6(T_6)$ = at-sensor registered radiance ($Wm^{-2}sr^{-1}\mu m^{-1}$).

$B_6(T_6)$ can be derived as following based on Planck's radiation formula:

$$B_6(T_6) = \frac{c_1}{\lambda^5\left[\exp\left(\frac{c_2}{\lambda T}\right) - 1\right]} , \qquad (4.6)$$

Where

c_1 =1.9104*10^10^ ($\mu Wcm^{-2}sr^{-1}\mu m^{-1}$)-$\mu m^5$

c_2= 14387.7 μm-K are radiation constants

T = surface temperature. (Spectral radiance unit: $\mu Wcm^{-2}sr^{-1}\mu m^{-1}$=0.01 $\mu Wcm^{-2}sr^{-1}\mu m^{-1}$)

Considering the altitude from which Landsat TM/ETM+ is located; at –sensor registered radiance is not explicitly direct from the target because upwelling emitted ground signal leaving the target is attenuated and enhanced by the atmosphere (Qin, 2001). Due to these atmospheric effects or path radiance, at-sensor received radiance can be expressed as following:

$$B_6(T_6) = \tau_6\left[\varepsilon_6 B_6(T_s) + (1-\varepsilon_6)I_6^{\infty}\right] + I_6^{\uparrow} \qquad (4.7)$$

Where

T_s = land surface Temperature [K],

T_6 = brightness temperature at band 6 [$Wm^{-2} sr^{-1}nm^{-1}$],

τ_6 = atmospheric transmittance at band 6 [-],

ε_6 = surface emissivity [-],

$B_6(T_6)$ = at-sensor registered radiance [$Wm^{-2} sr^{-1}nm^{-1}$],

I_6^{∞} = down welling irradiance [$Wm^{-2} nm^{-1}$],

$I_6^{\uparrow}$ = upwelling radiance [$Wm^{-2} sr^{-1}nm^{-1}$].

According to Qin *et al.,* (2001), upwelling radiance and downwelling atmospheric radiance can be obtained by following the method by Franca *et al.,* (1994) or by using the mean value theorem approach by Prata (1993) and Coll (1994). However, for this study all atmospheric parameters i.e., atmospheric transmittance, upwelling radiance and downwelling radiance were calculated from a Web-based Atmospheric Tool (ACT) (http://atmcorr.gsfc.nasa.gov/) which has been solely developed for Landsat (TM and ETM+) single-thermal bands (Barsi, 2007; Coll. *et al.*, 2010). This tool has been freely available online from 2000 to the present. For it to compute atmospheric correction parameters, the tool requires information on date, time and the location at which the image was acquired. According to Coll (2010), the tool incorporates atmospheric profiles as inputs of the MODTRAN-4 radiative transfer code from National Centers for

Environmental Predictions (NCEP) (Berk, 2000; Kalnay, 1996) to compute transmittance, upwelling radiance and downwelling radiance. On the other hand, surface emissivity value of 0.96 was used and the value was obtained from related work by Guarini *et al.,* (2010).

Aster thermal bands were atmospherically corrected using In- Scene Atmospheric Compensation algorithm (ISAC) implemented in ENVI (equation 4.6). The algorithm was adapted from the work of Johnson and Young (1998). The algorithm models the radiance at sensor from ground surface at each individual pixel. This was done by first searching for the TIR band with the highest brightness temperature from the TIR bands list. Then the band with the highest brightness temperature was used as reference. Following this method, TIR bands and the reference blackbody radiance values were plotted against the measured radiances (Johnson*, et al.*, 1998) and a line of fit was fitted on the highest points within the scatter (Young *et al.*, 2002). Upwelling atmospheric radiance and atmospheric transmission were derived through obtaining an estimate of surface temperature from each pixel within the dataset and constructing a scatterplot of radiance against brightness temperature.

4.3.3. Image Processing Tools

Environmental for Visualising Images (ENVI) and BEAM softwares were adopted for image processing and analysis. ENVI software is of significant importance as it allows visualisation, analysis of remote sensing data. The software has almost all the entire basic image processing functions as well as different interactive image analysis capabilities. Similarly, BEAM is an open source toolbox and development platform for visualising, analysing and processing of satellite remote sensing raster datasets specifically developed for Envisat's optical instruments (ESA, 2012).

4.3.4. Image Spatial Subsetting

All images were spatially sub-setted using image resizing tools in ENVI environment to limit their extent only to the region of interest before analysis. This process improved the processing time and enhanced the visibility of inherent features within the region of interest.

4.3.5. Nearest Neighbour Resampling Method

In order to implement the MPB primary productivity model; all the required variables were supposed to have the same spatial resolution. However, Photosynthetically Active Radiation (PAR) data from Modis Aqua had a spatial resolution of 1 km and 1.1 km from Sea WiFS. Contrastingly, the maximum rate of photosynthesis (P^B_{max}) determined based on temperature derived from Landsat (TM and ETM +) and Aster had a spatial resolution of 60 m and 90 m respectively, whereas chl-*a*+ phaeopigments concentrations from Landsat (TM and ETM+) had a 30 m spatial resolution and 15 m from Aster. Thus PAR and P^B_{max} datasets were resampled to 30 m and 15m spatial resolutions of chl-*a* derived from Landsat (TM and ETM+) and Aster, respectively using the nearest neighbour method. The nearest neighbour resampling method was used because it retains the actual pixel values from the original dataset. Finally, the resampled datasets was re-projected to the same map projections, which are UTM and a WGS-84 datum. As mentioned before, this was done as a pre-processing step towards implementing the MPB primary productivity model by Platt and Jassby (1976).

5. Classification of Intertidal Mudflat Sediment Types from Remote Sensing Data

This chapter presents methods which were implemented in determining different sediment types from intertidal mudflats and the results attained respectively. Figure 5-1 below illustrates the schematic methodological workflow that was adopted in this study to classify mudflats sediments on the basis of sediment properties.

5.1. Schematic Illustration of the Image Classification

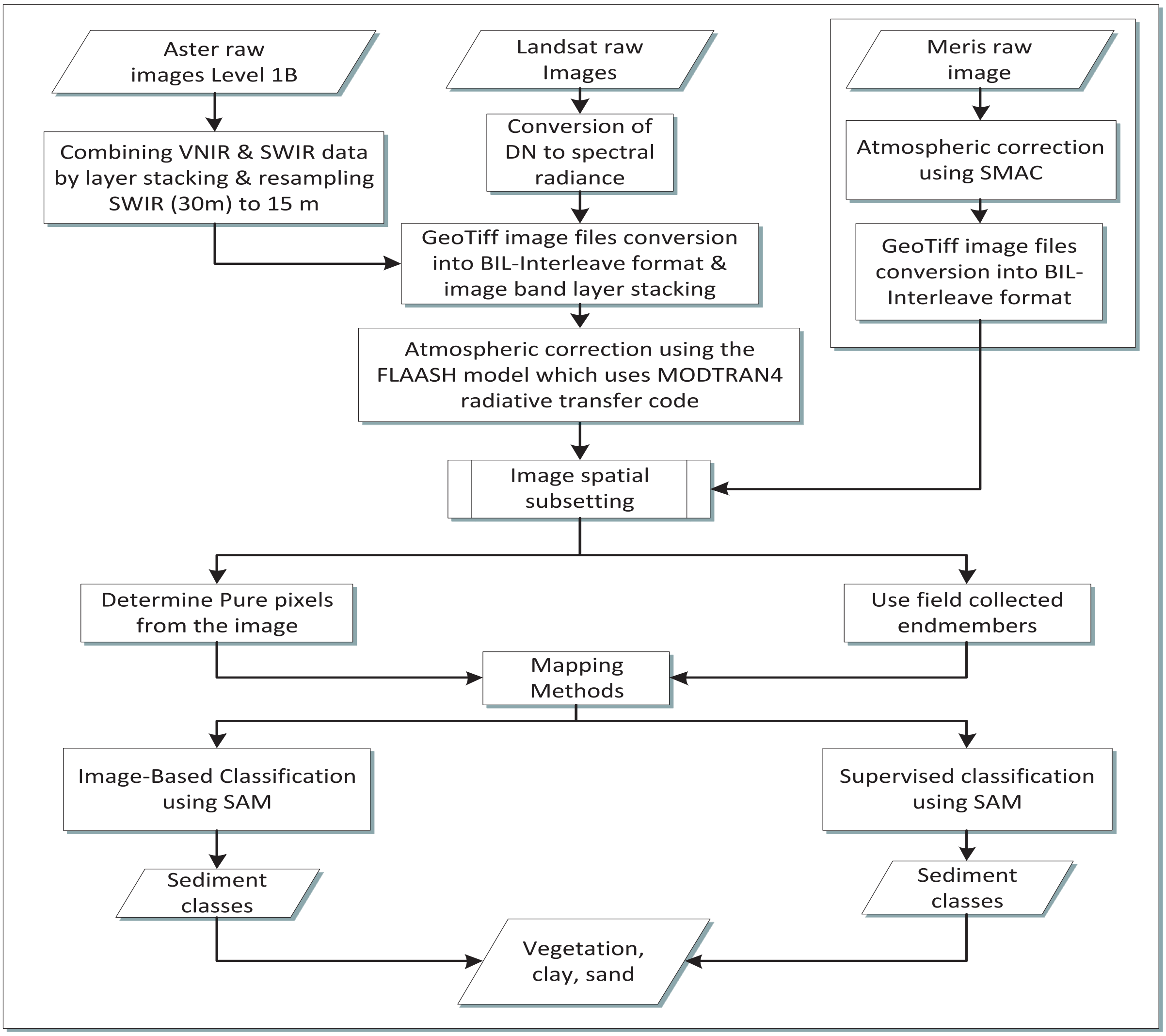

Figure 5-1: Research methods showing processing steps

Stal, (2010) defined intertidal mudflats as coastal zones that are frequently immersed and exposed according to the tidal cycle. These areas are normally characterised by different sediment types ranging from coarse sand with grain size stretching from 63 µm to 2 mm (Adam, *et al.*, 2009), to silt and fine clay or mud with particles less than 62.5 µm (Stal, 2010). For this study only two sediment types were considered, these being sand and clay. These sediments vary from place to place and time to time. Information on sediment types is crucial in understanding intertidal mudflat ecosystems functioning. The knowledge on sediment characteristics helps to understand the spatial and temporal variability in chl-*a* content and primary productivity within the area. Thus, in this study two methods were used to retrieve information on sediment particle size. The methods include (i) supervised classification and (ii) image based classification. The two methods were implemented based on Spectral Angle Mapper (SAM) algorithm; as illustrated figure 5-2. Only atmospherically corrected earth observation datasets were used in this study.

5.2. Supervised and Image Based Classification using Remote Sensing Data

Supervised classification is a method for grouping image pixels in a dataset into classes corresponding to the user-defined training classes based on field collected endmembers. On the other hand, the physical based image classification method, classifies the image by grouping pixels in a dataset using only image extracted endmembers determined through Pure Pixel Index (PPI). In this study, physical image based classification will also be referred to as unsupervised classification. The two methods were implemented using spectral angle mapper (SAM) algorithm (Boardman *et al.*, 1994; Brotas*, et al.*, 1995).

Image based classification was done based on image extracted endmembers. Derivation of endmembers from remote sensing data was done using the PPI. However, before this algorithm was implemented, we firstly reduced the inherent remote sensing data dimensionality using Minimum Noise Fraction (MNF) transformation method (Boardman*, et al.*, 1994). According to Boardman and Kruse, (1994) the MNF transformation method defines the inherent data dimensionality through separating and equally distributing the noise within data. Following this method, the resultant bands were ordered such that a larger amount of variance was within the first few bands. The actually variance declined with an increase in the number of bands. The decrease in data variance continued until only noise and none coherent image bands remained. According to Green *et al.,* (1988) this method produces better results as compared to field determined endmembers as the image spectra accurately accounts for any errors in calibration. In addition, the method was significant as it lessened further spectral computational complications on the data to be analysed, thereby improving further spectral data analysis results (Green*, et al.*, 1988).

PPI is one of the multi-spectral endmember extraction algorithms that has been developed by Boardman *et al.,* (1994). The method was selected because: (i) it derives spectral endmembers based on the inherent remote sensing data dimensionality and (ii) derived endmembers were the product of repeated and subsequent iterations. This procedure makes endmembers to be suitable and pure (Chaudhry *et al.*, 2006; Chein *et al.*, 2004). For this study, a value of 19.5 for the number of PPI, and a PPI threshold value of 8.5 was used. The smaller number of PPI was selected because it showed only purest pixels as compared to a large number. The PPI computation identified and grouped purest pixels in the n-dimensional space. The purest pixels are usually associated with bright pixels in the image (Chaudhry*, et al.*, 2006).

5.2.1. SAM Algorithm

Selected remote sensing images were classified using SAM algorithm (fig 5.1)(Green*, et al.*, 1988). The algorithm classifies images by comparing the unknown image spectra with the known spectra (De Carvalho*, et al.*, 2000; Kruse *et al.*, 1992). In this case the known spectra refer to field determined and image extracted endmembers. The resultant outputs of SAM, were classified images with the best match at each pixel, measured in radians ranging from 0 to $\pi/2$ (Kruse *et al.*, 1993). According to Kerle *et al.,* (2004) and Kruse *et al.,* (1993) the approach is rather a qualitative measure for comparing known and unknown spectra. However, the quality of image classification is rather a function of endmembers purity.

Like any other classification method SAM algorithm has its own advantages. SAM algorithm is considered as simple and quick in mapping the spectral similarity between the unknown *(r)* and the known spectra *(t)* (fig 5-3) (Yuhas*, et al.*, 1992). The main advantage of SAM is that, it is independent of brightness. This method is good at suppressing background or shading effects thereby enhancing reflectance characteristics of the intended feature (De Carvalho*, et al.*, 2000). During computation the algorithm takes the arccosine of the dot product of the spectra (Kruse*, et al.*, 1993). For this study, a maximum angle of 0.15 was used. A small angle was preferred as it demonstrates closer, fewer and better matches to the reference spectra. Usually, a large angle results in a more spatially coherent image but largely associated with poor pixel matches as compared to a low threshold angle.

Despite the above mentioned advantages, SAM has some drawbacks as well. For example, the technique is basically not sensitive to illumination (Kruse*, et al.*, 1993). It only uses the vector direction instead of the vector length during computation. When dealing with the problem of image spectral mixing the method is having some problems. Under normal circumstances the earth's surface is heterogeneous and the presence of mixed pixels is indisputable. In fact, it assumes that endmembers selected to classify the image are a true representation of the pure spectra of the target (De Carvalho*, et al.*, 2000).

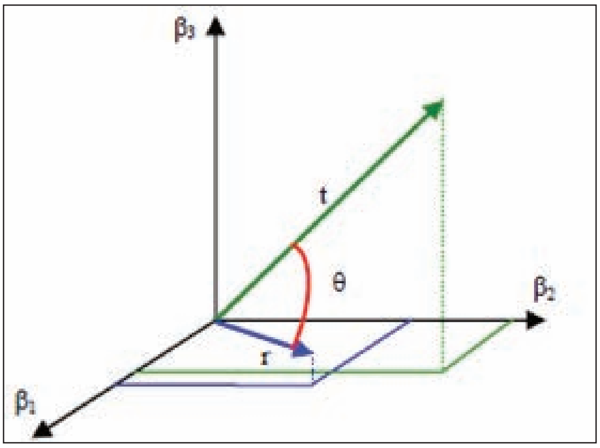

Figure 5-2: SAM algorithm Concept

The SAM algorithm is expressed as following:

$$\alpha = \cos^{-1}\left(\frac{\sum_{t=1}^{nb} t_i r_i}{\sqrt{\sum_{t=1} t_i^2 \sum_{r=1} r_i^2}}\right), \qquad (5.1)$$

Where

nb = number of bands

t_i = unknown spectra

r_i = known spectra.

6. Results and Discussions of Sediment Classification

As a pre-ample, the following chapter illustrates some of the research findings in this study. The results include determined spectral reflectances from different sediment types. Sediment classification results are also demonstrated from both image based classification using image extracted endmembers and supervised classification based on field collected endmembers. From image based classification statistical tables are also illustrated for all the selected images.

6.1. Ground Determined Spectral Reflectance Curves

The results in figure 6-1 shows spectral signature of sea weeds, with low reflectance in the green visible band and high reflectance in the near infra-red band with a steep red edge between the visible and near infra-red bands. Low reflectance in the visible spectral region confirms a strong absorption by chlorophyll pigments, whereas a relatively high reflectance in the near-infra-red is as result of the leaf's internal scattering and no absorption. This spectral trend implies that vegetation have high concentrations of photosynthetic pigments that absorb light in the visible range at the same time reflecting much in the longer wavelength.

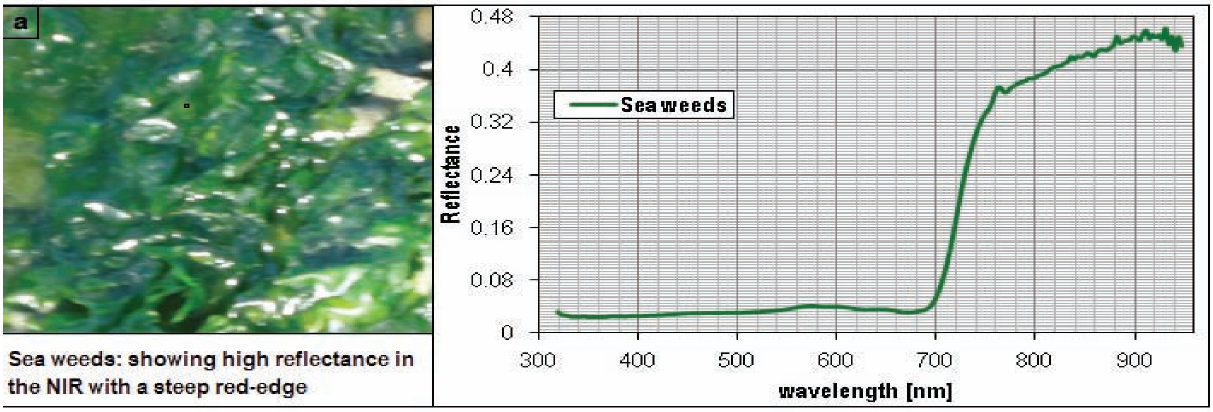

Figure 6-1: Spectral signature for sea weeds in intertidal mudflats of Wadden Sea

The result in figure 6-2 displays a steep rise in the reflectance spectum of clay sediments with algae betweeen 400-550 nm, with a strong chl-*a* absorption dip at 673 nm. However at 700 nm, the reflectance spectra is somehow smooth without much change meaning the spectra is not affected by MPB presence. This spectral dip at 673 nm is expected and largely explained by the presence of microphytobenthic diatoms /or organisms in clay sediments which greatly contribute to the mudflat biomass. These results are consistent with the work of Adam*, et al.,* (2009) who from field measurements using ASD spectrometer, observed similar spectral behaviour of clay sediments, with high absorption around 673 nm. Actually, when there is no microphytobenthic biomass content within sediments, the spectral profile will be somehow smooth indicating no absorption troughs (fig 6-3). Similar observations were made by Kromkamp, *et al.,* (2006) who found that sediments dominated by MPB diatoms have a sharp spectral reflectance at around 500 nm with an absorption dip at 675 nm resulting from chl-*a* absorption at that wavelength.

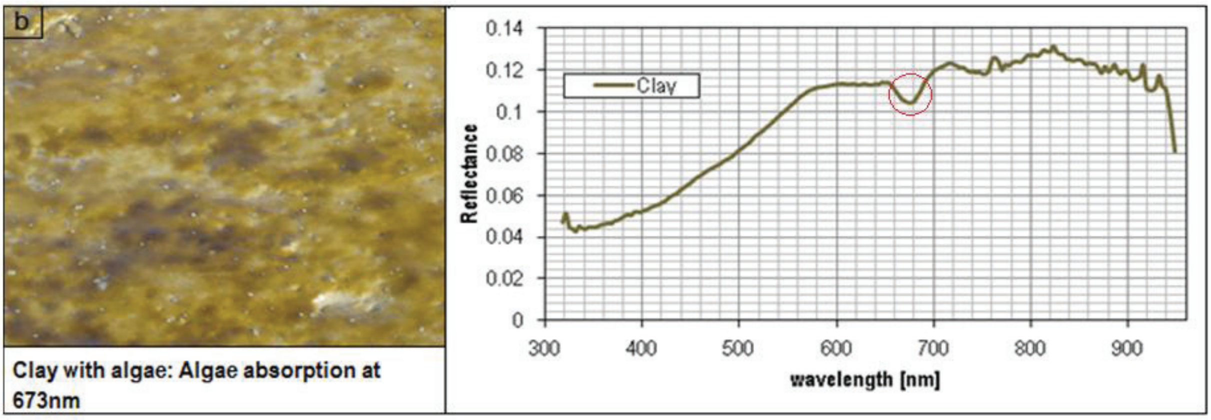

Figure 6-2: Spectral signature for clay sediments in intetrtidal mudflats of Wadden Sea

Sand sediments spectral reflectance results displayed in figure 6-3 demonstrate a different spectral signature than the one observed in figure 6-2. Unlike in clay sediments, the result from figure 6-3 shows an almost smooth spectral reflectance signature of sand sediments. This observation is attributed to less microphytobenthic content in sand sediments. This remark is also confirmed by a smooth trend in the spectral reflectance profile with less chlorophyll absorption dip at 673 nm throughout the spectral range as observed in the figure below. However, there exist minor absorption residuals at around 673 nm that can be attributed to the limited presence of MPB diatoms in sandy sediments. In general, a clear cut distinction amongst different endmembers from different sediment classes is observed. These differences can be attributed to the variability in algal /or MPB content available in different sediment types. According to Carrère *et al.,* (2004) the amount of absorption in different sediment spectra is directly a function of pigment chl-*a* concentration detected in different sediment types.

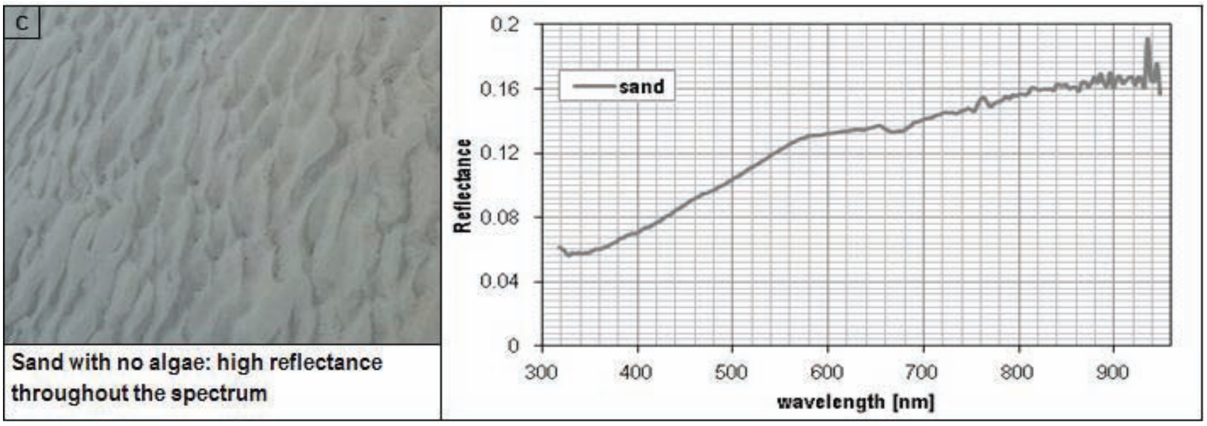

Figure 6-3: Spectral signature for sand sediments in intertidal mudflats of Wadden Sea

6.2. Derived Sediment Classes from Supervised and Image Based Classification

This section demonstrates sediment classes attained from image based classification and supervised classification. Sand and clay sediments from the top layer of intertidal mudflats were largely derived from remote sensing data based on their spectral signatures.

Derived information on sediment classes shows that clay and sand sediments vary spatially across the entire intertidal mudflats of the Wadden Sea. On the other hand, a close examination of sediment top layer classification results shows that clay sediments are less in spatial extent as compared to sand sediments which seem to occupy a large area in all the results. It can also be realized that in year 2000 there was a more pronounced clay and sand content over the entire Wadden Sea area (fig 6-4). It can also be observed that across the entire region sandier and clay sediments were detected in the north eastern and south western regions. Limited detections were made in the central region of the Wadden Sea probably due to high water levels submerging the mudflats during the satellite overpass period.

In addition, from both image based classification and supervised classification results; it can be as well observed that more clay sediments have been derived from the image based classification method than the later except from figure 6-9. In figure 6-9 the results from both image based classification and supervised classification demonstrates a similar distribution of sand and clay sediments although not giving a one-on-one match-up. This observation can be attributed to the fact that field collected endmembers may be affected by the prevailing environmental factors. For instances, the presence of thin water films /or water content, mixed sediment properties, can largely compromise the purity field collected spectral endmembers. However, this limitation can be improved either through undertaking laboratory analysis of sediment reflectance spectral signatures (Schwengerdt, 1997) /or by using analytical methods like X-ray or microprobe analysis (Clark *et al.*, 1993; DerondeKempeneer *et al.*, 2006) because these procedures would minimize the influence of environmental factors on reflectance. However, the fact that imaged based classification may have overestimated the sediments content within intertidal mudflats may not be ruled out.

Derived sediment classification results from the two classification methods, show a similar spatial distribution with those of chl-*a* distribution in figure 8-1. This finding is generally acceptable because clay particles are largely associated with high microphytobenthic biomass content than sand sediments. This is because clay sediments are characterized with fine cohesive and stable particles generally associated with high nutrient content whereas sandy sediments are mostly affected by hydrodynamic processes such as tidal currents that cause re-suspension of sediment particles (Delgado *et al.*, 1991; MacIntyre. *et al.*, 1996; Sundback*, et al.*, 1991). Thus this uniqueness probably contributes towards high MPB biomass in clay (Herman *et al.*, 2001).

A summary of statistics was also computed from all the physical based classification results to assess the accuracy of the classification. The maximum NDVI values were also determined for each derived sediment class. It can be noted that NDVI values are high on vegetation followed by those on clay sediments which is largely expected due to various reasons mentioned before. For all the statistical results derived from image based classification, the maximum values were recorded on sand sediments and the minimum values on clay sediments.

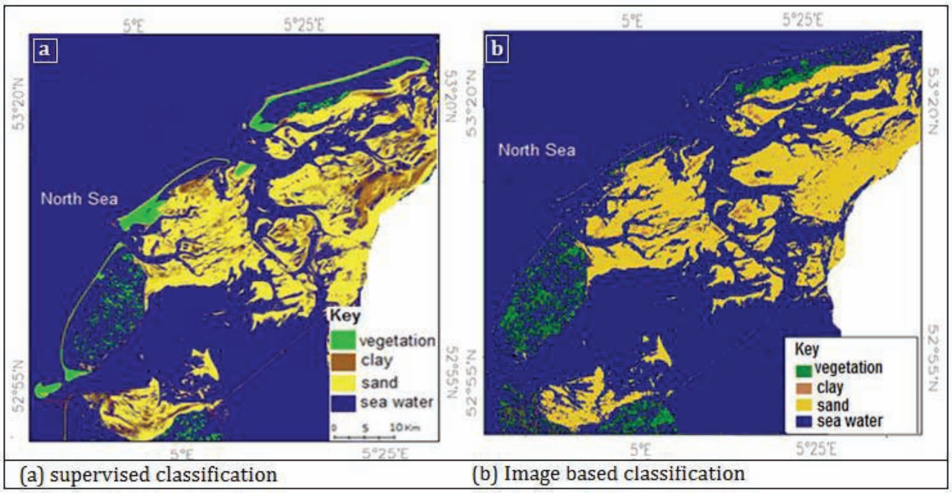

Figure 6-4: Intertidal mudflats sediment classes derived from Landsat 2000 using SAM

Table 6-1: Summary of statistical tables for unsupervised classification from Landsat 2000

	Min	Max	Mean	Stdev	ndvi
vegetation	1.00	7.00	5.68	2.49	0.71
clay	0.01	2.00	1.98	0.21	0.28
sand	2.00	5.00	5.98	0.03	0.02

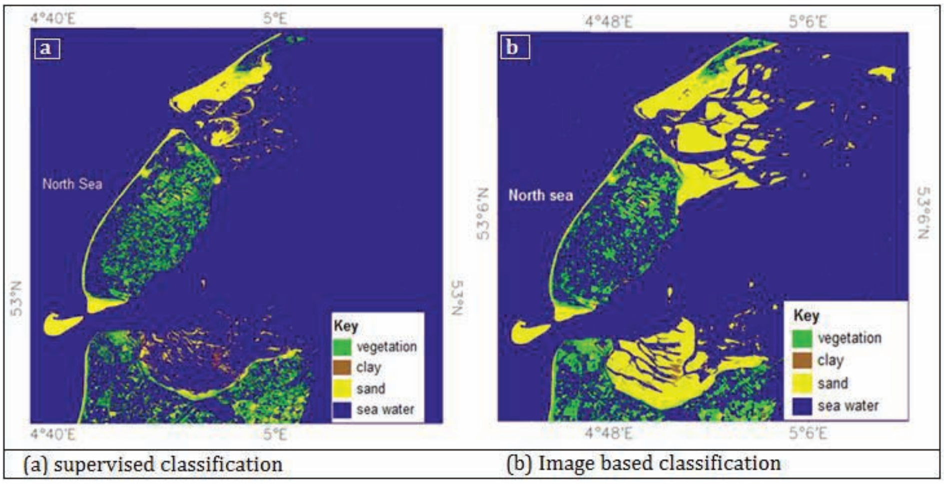

Figure 6-5: Intertidal mudflats sediment classes derived from Landsat 2003 using SAM

Table 6-2: Summary of statistical tables for unsupervised classification from Aster 2003

	Min	Max	Mean	Stdev	ndvi
vegetation	0.00	9.00	2.54	2.87	0.69
clay	0.00	6.00	1.17	0.88	0.25
sand	2.00	10.0	9.99	0.25	0.018

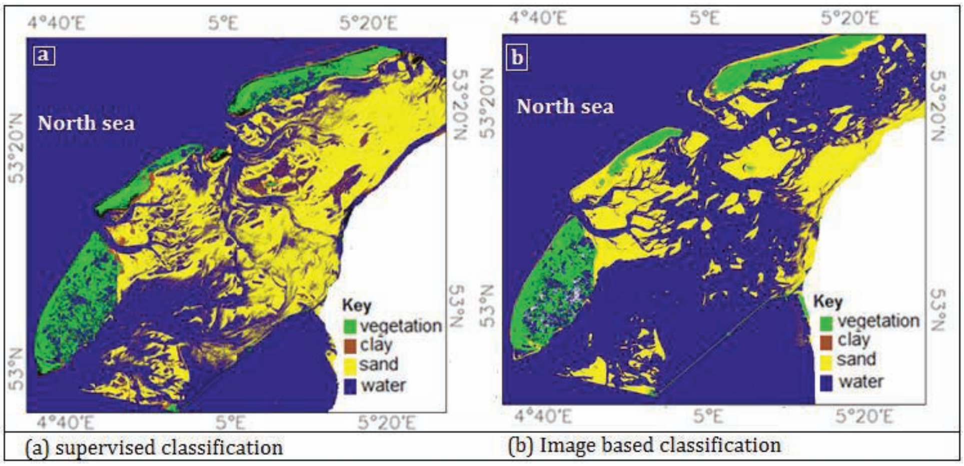

Figure 6-6: Intertidal mudflats sediment classes derived from Aster 2007 using SAM

Table 6-3: Statistical table summary for image based classification from Aster 2007

	Min	Max	Mean	Stdev	ndvi
vegetation	0.00	8.00	7.98	0.41	0.65
clay	0.00	2.00	1.68	0.67	0.23
sand	1.00	7.00	7.00	0.08	0.016

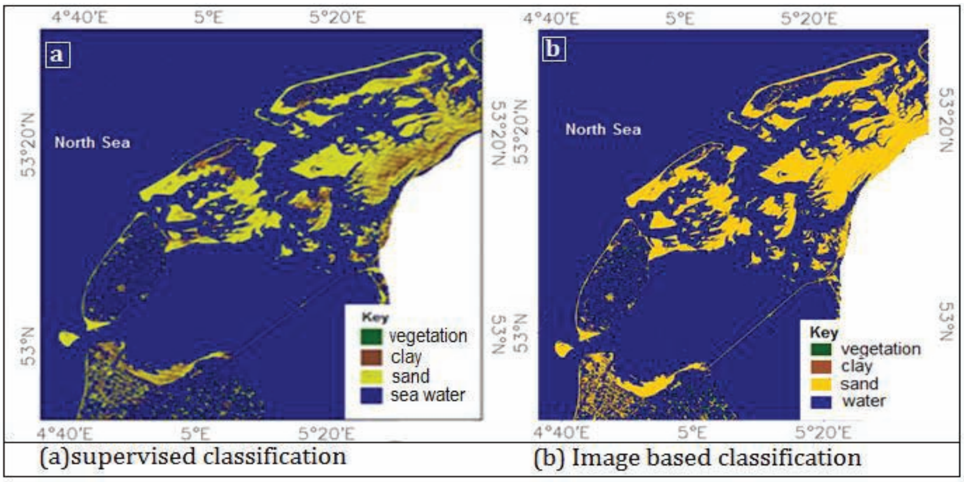

Figure 6-7: Intertidal mudflats sediment classes derived from Landsat TM 2009 using SAM.

Table 6-4: Summary of statistical tables for unsupervised classification from Landsat 2009

	Min	Max	Mean	Stdev	ndvi
vegetation	0.00	5.00	4.34	1.79	0.50
Clay	0.00	3.00	2.16	0.37	0.25
Sand	2.00	6.00	5.87	0.611	0.01

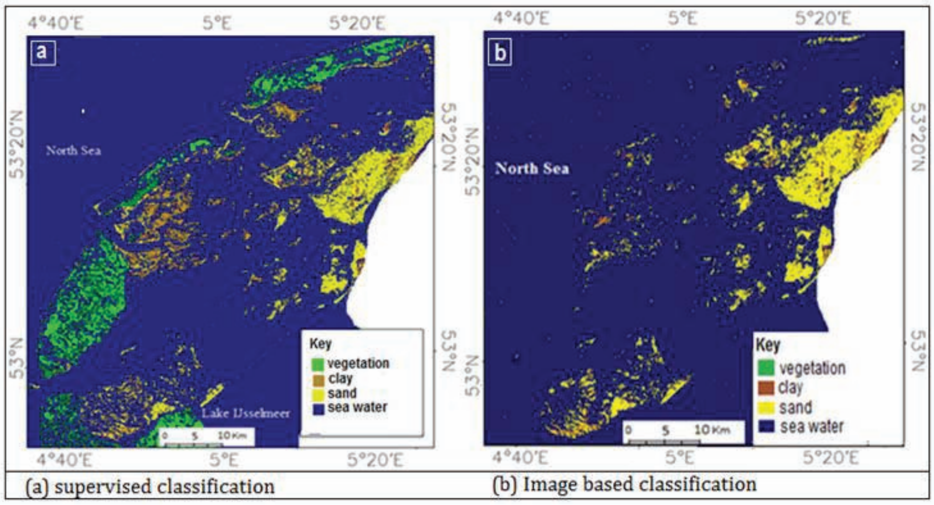

Figure 6-8: Intertidal mudflats sediment classes derived from Landsat TM 2010 using SAM

Table 6-5: Statistical table summary for image based classification from Landsat TM 2010

	Min	Max	Mean	Stdev	ndvi
vegetation	0.00	4.00	0.92	1.75	0.40
Clay	0.01	7.00	2.47	1.51	0.21
Sand	0.00	9.00	8.74	1.53	0.02

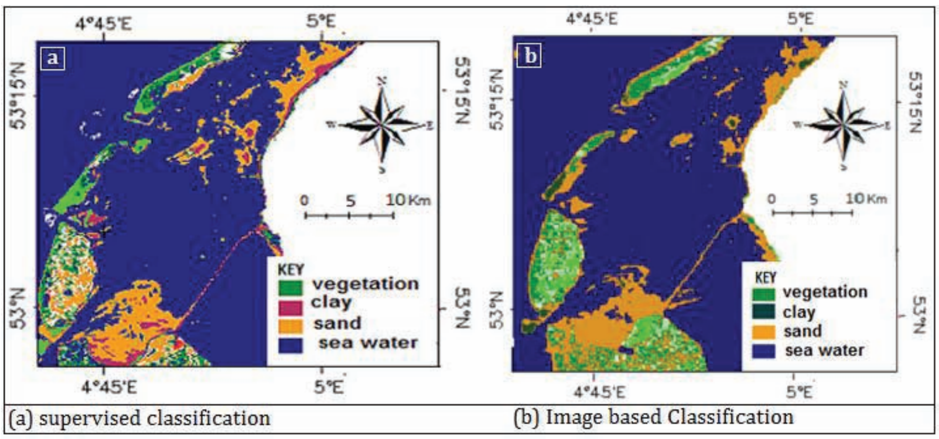

Figure 6-9: Intertidal mudflats sediment classes derived from Meris 2011 using SAM

Table 6-6: Statistical table summary for image based classification from Meris 2011

	Min	Max	Mean	Stdev	ndvi
vegetation	0.10	12.0	9.30	2.41	0.37
Clay	0.60	7.97	2.47	0.35	0.13
Sand	1.00	10.0	7.49	2.53	0.03

According to MacIntyre *et al.,* (1996), deriving information on different sediment types is very crucial in understanding the horizontal spatially distribution of chl-*a* and the primary productivity of microphytobenthic diatoms in in intertidal mudflats. This assertion holds as we can observe a comparable distribution from derived chl-*a* and primary productivity maps illustrated in figure 8-1 and figure 8-4 respectively with the results shown above. The derived sediment classes play a significant role in explaining the observed distribution of chl-*a* and primary productivity based on the knowledge we have on sediment morphological characteristics like available nutrient content.

7. Deriving Microphytobenthic Primary Productivity from Intertidal Mudflats

Microphytobenthic (MPB) organisms are a composition of benthic unicellular microscopic organisms forming biofilms on intertidal sediment areas (Paterson*, et al.*, 2001). So far, microphytobenthic diatoms are one of the most organisms determining intertidal mudflat primary productivity, as such they contribute significantly to estuarine food web. In fact, they are one of the main food producers for higher trophic levels in intertidal food chains.

7.1. Microphytobenthic Primary Productivity

In this study, MPB primary productivity was estimated from Landsat (TM and ETM+) and Aster remote sensing datasets with Meris being excluded. Normally, MPB primary productivity estimation can be done by using different models and each model has its own drawbacks. However, comparing different models is out of the scope of this study. Based on inference from previous literature, we found that the model by Platt and Jassby (1976) gives a better estimate and understanding of MPB primary productivity of the intertidal mudflats (Barranguet 1998). The model has been widely used in understanding MPB primary productivity of the delicate intertidal sediment surfaces in different areas (Barranguet*., et al.*, 2000). Thus, because of this reason the model by Platt and Jassby (1976) as illustrated in equation 7.1 has been adopted. The model computes MPB primary productivity based on a few environmental variables. These include chl-*a*, light intensity, maximum rate of photosynthesis at saturating irradiance (P^B_{max}), and initial slope (α^B) which is the measure of photosynthetic efficiency. To obtain actual estimates of these variables, various methods have been employed as shown below. Figure 7-1 demonstrates a summarized procedure that was followed to derive MPB primary productivity from intertidal mudflats of the Wadden Sea area.

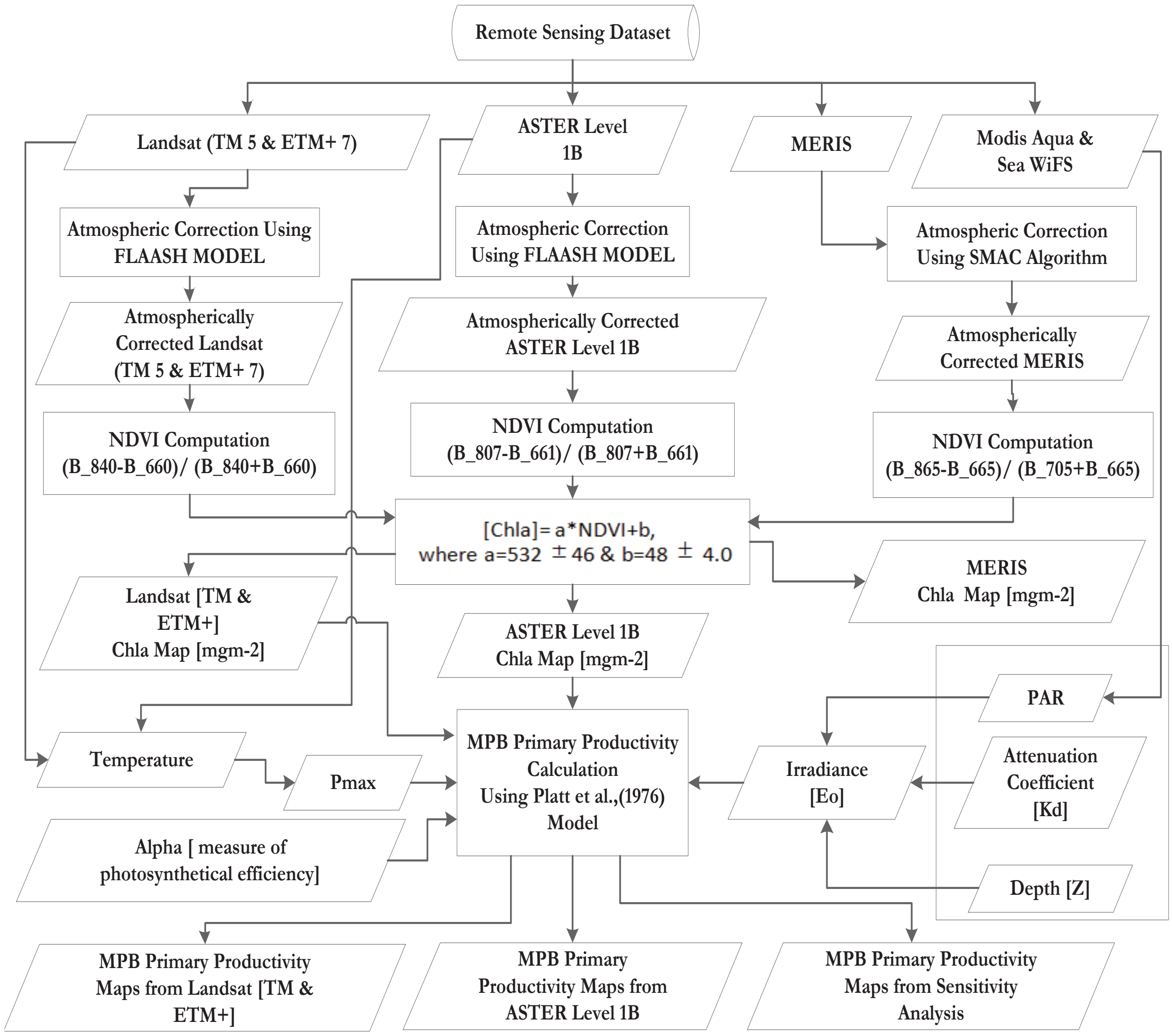

Figure 7-1: Schematic Procedure for deriving MPB primary productivity in the Wadden Sea

7.2. Primary Productivity Model

MPB Primary productivity model by Platt and Jassby,(1976) is expressed as following:

$$P = chla \cdot P^B_{\max}\left(1 - e^{\left(\alpha^B \cdot E_0 / P^B_{\max}\right)}\right) \tag{7.1}$$

The equation describes the rate of photosynthesis as a function of E_0 which is the incident light intensity (µmol m^{-2} s^{-1}) where P^B_{max} is the maximum rate of photosynthesis per mg chl-*a* (mg C mg chl a^{-1} h^{-1}), chl-*a* is chlorophyll a concentration, and α^B is a measure of the photosynthetic efficiency (mg C chl a^{-1} (µmol m^{-2} $s^{-1})^{-1}$ h^{-1}).

7.3. Derivation of Primary Productivity Coefficients

7.3.1. Chlorophyll *a* Estimation from NDVI

Chl-*a*+ phaeo (phaeopigments) was derived from normalized difference vegetation index (NDVI) using the regression equation by Kromkamp *et al.,* (2006) established between NDVI and [chl-*a*+phaeo] (mg.m-

^{2}) expressed as following: [chl-*a*]= a*NDVI+b, where a=532 $\pm$ 46 and b=48 $\pm$ 4.0 (95% confidence intervals), p (a,b) < 0.0001, number of points=307, r^2=0.67.

NDVI is a numerical indicator often used as a proxy for estimating mudflats chl-*a* concentration from remotely sensed data (Kromkamp*, et al.*, 2006). In analysing remote sensing data; the index uses the visible (VIS) red band (0.4-0.7 μm) and near-infrared (NIR) bands (0.75-1.1 μm) of the electromagnetic spectrum (Rulinda *et al.*, 2010; Tucker, 1979). The index was first applied by Rouse, *et al.,* (1973). Since then, the index has been successfully applied in rangeland assessment, crop yield estimation, as well as in drought prediction studies (Lei *et al.*, 2010; Minor *et al.*, 1999; Prasad *et al.*, 2006).

The index determines chl-*a* concentration based on the difference between the NIR and the red reflectance (equation 7.2). When the difference is large it means the concentration of chl-*a* is very high and the reverse is true. According to Rulinda *et al.,* (2010) NDVI values ranging from -1 through 0 to 1. In our case, the negative values symbolize water, values around zero for bare soil and values around one represent high mudflats MPB concentrations. However, in dense biomass concentrations the index tends to reach saturation. The index is defined by the following equation:

$$NDVI = \frac{\rho_{NIR} - \rho_{RED}}{\rho_{NIR} + \rho_{RED}} \tag{7.2}$$

Where

ρ_{NIR} = chl-*a* maximum reflectance in the near-infrared wavelength;

ρ_{RED} = maximum absorption in the red band.

Thus, based on the above equation, NDVI was calculated from the three atmospherically corrected remote sensing datasets as following:

Landsat	=	(B_840-B_660)/ (B_840+B_660);
Aster	=	(B_807-B_661)/ (B_807+B_661);
Meris	=	(B_865-B_665)/ (B_705+B_665).

7.3.2. Land Surface Temperature Retrieval from Landsat TIR Bands

P^B_{max} is a function of temperature, an increase in temperature results in an increase in P^B_{max}. Therefore, land surface temperature (LST) was derived from Landsat thermal bands (fig 7-2). To retrieve LST, we had to solve for T_s from equation 4.7, but before this step was applied, radiance at the surface was first computed following the equation below:

$$B_6(T_s) = [B_6(T_6) - I_6^{\uparrow} - \tau_6(1-\varepsilon_6)I_6^{\infty}] / \varepsilon_6\tau_6 \tag{7. 3}$$

Following this method, LST was then retrieved by inverting the Planck's law similarly as stated in 4.5 but now using radiance value at the ground *($B_6(T_6)$)* calculated from equation 7.3 (Coll*., et al.*, 2010; Qin, 2001).

7.3.3. Land Surface Temperature Retrieval from Aster TIR Bands

Temperature was extracted from atmospherically corrected Aster image products using the emissivity normalization technique which is implemented in ENVI (fig 7-2) (Hook *et al.*, 1992; Kealy *et al.*, 1993). The method computes temperature for every pixel and channel; assuming a surface emissivity value of

0.96 (Gillespie, 1985; Hook*, et al.*, 1992; Kealy*, et al.*, 1993). Emissivity values were computed based on the Planck's function (Eq. 4.6) from the highest temperature values for each pixel provided in the TIR dataset. The resultant outputs from this algorithm were five emissivity channels and the temperature.

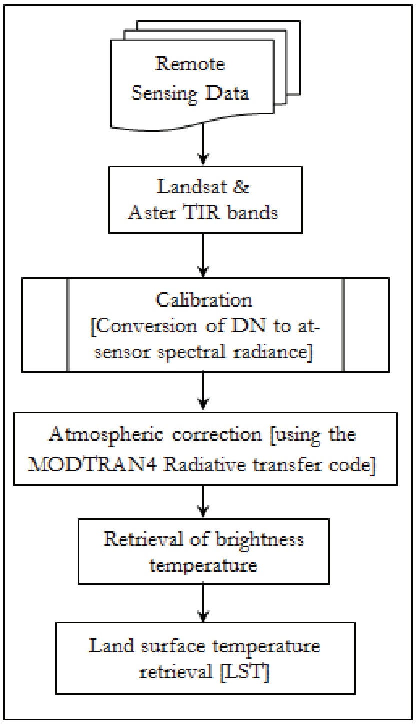

Figure 7-2: Schematic illustration of land surface temperature retrieval procedure from Landsat and Aster.

7.3.4. Light Intensity

Light intensity is again one of the major components of the primary productivity model. The light intensity at depth Z was derived by following the Lambert beer law (eq 7.4).To obtain light intensity, we used estimates mean for Kd, z coefficients and these coefficients were varied as explained in section 7.4 for sensitivity analysis. These coefficients were determined as highlighted in section 7.3.5.

$$E_0 = par \cdot e^{-k \cdot z} \tag{7.4}$$

Where

E_0 = light intensity (µmol m^{-2} s^{-1}) at depth *Z* (mm);

par = available photosynthetic active radiation (Einstein m^{-2} h^{-1}) at the mud surface;

k = attenuation coefficient (mm^{-1});

z = depth (mm).

On the other hand, Photosynthetic Active Radiation (PAR) in equation 7.4 is a very significant determinant of MPB primary productivity in intertidal mudflats ecosystems. For this study, PAR (400-700 nm) data was obtained from the ocean colour website; an online readily available global archive that was accessed via http://oceancolor.gsfc.nasa.gov/. The archive provides ready products from Modis Aqua and Modis Terra, CZCS, OCTS (ADEOS), SeaWiFS, and Meris (Envisat) satellites; with a spatial resolution of 1000 m and a swath of 2330 km (NASA, 2002).

For this study, only data from Modis Aqua and SeaWiFS was used. The data corresponding to the images acquired as outlined in table 3.3 except for Meris image as it was not used in primary productivity estimation. The archive provides daily data with each image having 23 bands. The bands include PAR in Einstein m^{-2} d^{-1}, from year 2002 to the present whereas; SeaWiFS data is available from 1997 till present. From SeaWiFS only data for 2000/05/13 was downloaded as it was not available from Modis Aqua. SeaWiFS has a spatial resolution of 1100 m and swath for 2806 km (Acker, 1997). The data was re-projected to Geographic (lat/lon) WGS84.

7.3.5. Maximum Rate of Photosynthesis (P^B_{max})

Field measured data for α^B, Kd and P^B_{max} was obtained through personal communication with Jacco Kromkamp (NIOZ-Yerseke). The dataset consisted of 374 samples and was used to derive the coefficients for the above mentioned variables so as to run the primary productivity model. From the raw dataset we derived a model for estimating P^B_{max} based on temperature and $P^B_{max.}$ To derive this algorithm; we had to filtered the data, by establishing a linear function between temperature and P^B_{max} using a 5th order polynomial function. From the polynomial function an estimate of P^B_{max} was then computed. Relative error (RE) of the 5th polynomial function was computed as following:

$$RE = \left(\frac{P^B{}_{\max\_measured} - P^B{}_{\max\_predicted}}{P^B_{\max\_measured}} \right) * 100, \qquad (7.5)$$

Outliers or extreme data values that is, values above or below 35 (±35 %) were filtered. This range has been selected in accordance to the recommendation of the satellite chl-*a* products (Bailey *et al.*, 2006). A linear relationship between temperature and P^B_{max} was derived based on filtered data. The following equation was attained y = 03242x-85.789 with 0.71 R^2 value. This equation was used to derive P^B_{max} using land surface temperature derived from remote sensing data.

After deriving α^B, Kd and P^B_{max} coefficients, MPB primary productivity at first stage was estimated by assuming a homogeneous distribution of microphytobenthic biomass at 2 mm depth, using a mean α^B value of 0.0264 and mean Kd of 1.607. The 2 mm depth was selected because normal that is where the maximum concentration of microphytobenthic organisms is attained. According to Jesus *et al.,* (2006) 2 mm depth is were light penetration is critical for biomass distribution. Most studies have been estimating primary productivity using this depth as reference. When compared with literature, the α^B value stated above is acceptable since it lies between 0.015 and 0.035 mg C chl a^{-1} (µmol m^{-2} s^{-1})$^{-1}$ h^{-1} as outlined by Barranguet. *et al.,* (2000).

7.4. Model Sensitivity Analysis

According to Saltelli *et al.,* (2008), sensitivity analysis (SA) is actually the assessment of how the model output variability can be explained by the variability in model inputs. Thus, for this study, SA was done to assess the performance and limitations of the primary productivity model by Platt and Jassby, (1976). Varying different variables was a significant step in understanding how these variables affected intertidal mudflat MPB Primary Productivity. The following variables were examined: maximum photosynthetic efficiency (α^B), sediment attenuation effect (K_d) and euphotic depth (Z mm) (table 7-1). For α^B and Kd the increament was based on the standard deviation computed from the raw data sets. In this thesis, euphotic depth is the depth at which the light intensity within the sediment profile is equal to 1% of the amount received at the surface (Scheffer, 2001). Euphotic depth is one of the critical factors controlling MPB biomass in intertidal sediment surfaces, such that a change in depth results in an exponentially decrease in incident light (Kromkamp*, et al.*, 2006). When sediment depth increases the inherent concentration of MPB biomass decreases due increased absorption of or attenuation of light within the vertical sediment profiles (fig 7-3). Incident light is the most important factor in MPB primary productivity of the intertidal sediments; an increase in incident light results in an increase in MPB primary productivity and vice versa.

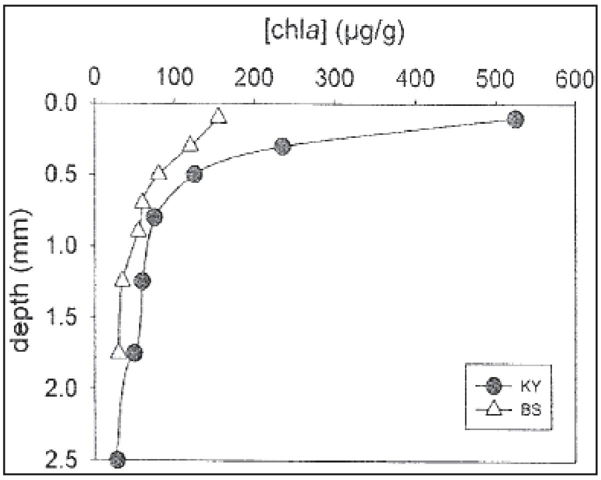

Figure 7-3: Two vertical distributions curves of chl-*a* within intertidal sediment surfaces with increase in sediment depth, adopted from Kromkamp. *et al.,* (2006) where profile KY the authors adopted from the works of Kelly *et al.,* (2000) and profile BS was taken from De Brouwer and Stal (2001)

Landsat image of the year 2000 was used for sensitivity analysis. Its selection was due to the fact that amongst all the images, the highest MPB primary productivity was detected on that date. Literature shows that MPB primary productivity occurs within a specific depth within sediment profile beyond which, its detection is difficult (Brotas*, et al.*, 1995). Therefore, we did sensitivity analysis by varying the sediment depths (mm). Thus, the vertical sediment profile depths of 2 mm, 5 mm and 7 mm were used. Their selection was based on findings from literature. According to Kromkamp*, et al.,* (2006), MPB primary productivity determination in the vertical sediment profile varies from 1 mm (Kromkamp. *et al.*, 1995), 2 mm (Pinckney *et al.*, 1991), 5 mm (Blanchard. *et al.*, 1995) and 10 mm (Brotas*, et al.*, 1995; MacIntyre.*, et al.*, 1996). Therefore, our selection of the three different sediment measurement depths was more or less guided by this literature.

Table 7-1: MPB Primary Productivity sensitivity analysis coefficients

Sensitivity Analysis Coefficients		
Variable	Mean value	Mean+ Stdev
Kd [mm^{-1}]	1.61	2.60
α^B [$\mu mol\ m^{-2}\ s^{-1}$]	0.026	0.04

Determined values of Kd seem to be within the range when compared to the diffuse attenuation coefficients compiled by MacIntyre (table 7.2). The table cited below indicates different Kd values and the amount of light attenuated at a given depth.

Table 7-2: Derived values of the sediment diffuse attenuation coefficients, Kd cited from MacIntyre*, et al.,*(1996).

Particle size [μm]	Sensor	Light [λ in nm]	Kd [mm^{-1}]	Depth of 1% Light level [mm]	Source
n.d	E.E.L Photoelectric cell	white	0.8-0.9	5.1-6.1	Hopkins (1963)
110	Pryheliometer	sunlight	0.7	6.9	Taylor (1963)
270	Pryheliometer	sunlight	0.8	5.9	Taylor & Gebelein (1966)
330			0.5	8.7	
330			0.4	13.2	
108-519	Selenium Photocell	white	0.6-3.9	1.8-7.7	Gomoiu (1967)
300	Photodiode	Blue	1.3	3.5	Fenchel & Straarup (1971)
		Red	1.0	4.7	
		Infrared	0.9	5.1	
		White	1.1	4.3	
90	Photodiode	400-700	11-15.4	0.3-0.4	Haardt & Neilson (1980)
105			7.3-9.2	0.5-0.6	
205			2.4-4.3	1.1-2.0	
260			1.5-2.8	1.7-3.0	
n.d	Li-Cor-Quantum Sensor	white	1.9-32.6	0.1-2.5	Colijn (1982)
Silt-clay	Fiber Optic Microprobe	450	20.3	0.2	Jorgensen & des Marais (1986)
		600	8.0	0.6	
		670	16.8	0.3	
		1,000	2.3	2.0	
<63	Fiber Optic Microprobe	400-700	3.5	1.3	Kuhl *et al.* (1994)
63-125			1.6	2.8	
125-250			1.6	2.8	
250-500			1.0	4.6	
145-165	ISCO Spectroradiometer	400	3.5-4.2	1.1-1.3	MacIntyre & Cullen (1995)
		700	4.9-5.6	0.8-0.9	

8. Results and Discussions of MPB Primary Productivity of the Intertidal Mudflats of the Wadden Sea

The following section displays the major research findings in this study. The results include the first derived primary productivity maps of the Wadden Sea as well as a presentation of chl-a + phaeo concentrations [mg.m^{-2}] derived from NDVI calculations following the work of Kromkamp, et al. (2006). Again, LST maps over the Wadden Sea retrieved from TIR bands of Aster and Landsat are also presented and discussed in this section, including P^B_{max} results determined from LST based on the following established mathematical model y=03242x-85.789 (fig 8-3). In addition, the effect of Kd, α^B and depth (Z mm) on microphytobenthic primary productivity is discussed in this chapter.

8.1. Chl-a+ Phaeopigments Concentration Derived from Different Sediment Types

The results from figure 8-1 illustrate derived chl-*a*+phaeo concentrations (mg.m^{-2}) from intertidal mudflats. The spatial and temporal variability of chl-*a*+ phaeo concentration (mg.m^{-2}) in intertidal mudflats are also presented. This variability is denoted by the presence of the patchy chl-*a*+ phaeo distributions across the entire Wadden Sea intertidal area. From the findings in figure 8-1, cool colours represent low chl-*a*+phaeo concentration whereas warm colours represent high concentration. On a temporal scale, it can be noted that high chl-*a* concentrations were recorded in the year 2000 and the minimum being in 2011. Brotas *et al.,* (1995) has categorical stated that the spatial variability of MPB biomass in intertidal mudflats is largely explained by sediment types. This assertion is further substantiated by the work of van der Wal *et al.,* (2010) whose results demonstrated that large scale patterns in MPB biomass distribution are a function of the existing geomorphological characteristics, sediment type, nutrient availability and tidal exposure time. Again, similar conclusions have also been drawn by Blanchard (2000) and Jesus*, et al.,* (2006). Actually, when compared with derived sediment classes in section 6.2 these assertions seem to be valid. Actually, this spatial heterogeneity is acceptable and agrees with previous literature, where this phenomenon is largely aligned to the prevailing environmental variables like sediment type, nutrient availability, and temperature.

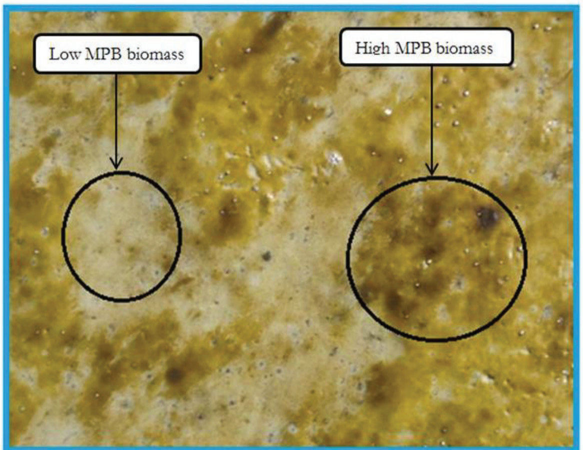

Patchy distribution of algae in clay sediments

Despite a clear spatial variability of MPB biomass in horizontal dimension of the top sediment layer amongst different sediment types (fig 8-1); a comparable distribution is also depicted within distinct sediment classes especial in clay sediments as can be seen on the picture on right side. Jesus *et al.,* (2005) has attributed this intra-sediment algal content variability to the vertical migration of MPB organisms within the vertical intertidal sediment profile. However, another perspective for intra-sediment epileptic diatom heterogeneity is basically owed to available clay content within the area. For example the existence of mixed sediment classes can greatly compromise nutrient content which is one of the determinants for microphytobenthic growth (Blanchard. *et al.*, 1997; van der Wal*., et al.*, 2010).

Moreover, the results in figure 8-1 indicate that derived chl-*a*+ phaeo concentrations ranges fluctuate between 0-182 mgm^{-2} from the Wadden Sea intertidal mudflats over the years. According to Brotas*, et al.,* (1995), this distribution in chl-*a* concentrations in intertidal mudflats is directly a function of two main factors that is sediment type and tidal height. The two control factors like temperature, salinity, irradiance, effects of tidal current, nutrient availability. Other research studies have also found that chl-*a* concentrations range between 0-520 mgm^{-2} in some sites and 50-200 mgm^{-2} along the French coast of the eastern English channel (Carrère*, et al.*, 2004) whereas Sundback. *et al.,* (Sundback. *et al.*, 1988) found chl-*a* ranges of 0-87mgm^{-2} in the Southeastern Kattegat. Whereas Brotas *et al.,* (1995) at the Tagus estuary he found chl-*a* concentrations ranging between 20-300mgm^{-2}. When comparing all these findings we can conclude that chl-*a* concentrations vary spatially, despite the conclusion drawn by Brotas who, based on tabulated chl-*a* data (table 8-1) stated that chl-*a* in temperate intertidal mudflats does not vary.

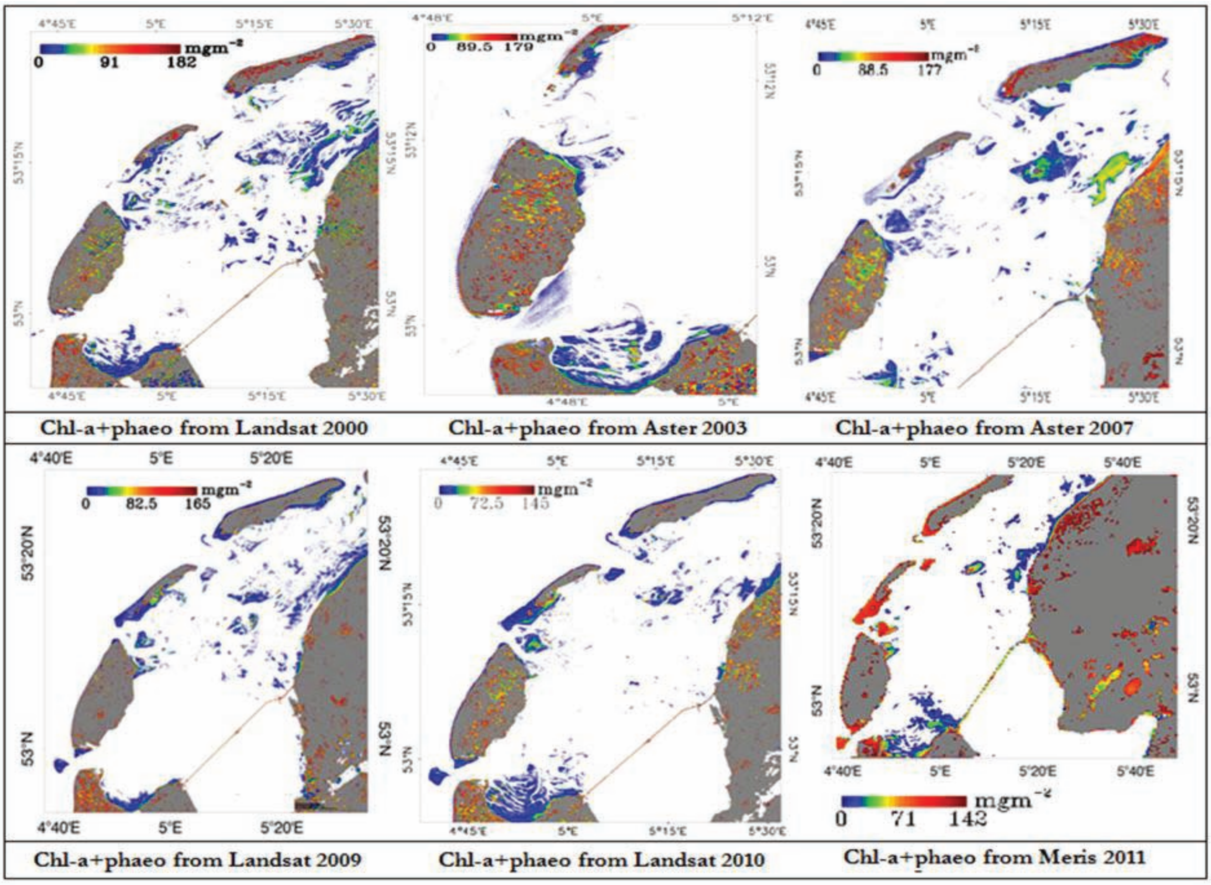

Figure 8-1: sediment chlorophyll *a* content (chl-*a*+phaeo, mg.m^{-2}) derived from the linear equation by Kromkamp *et al.,* (2006) for six different days in six different years.

Table 8-1: Chl-*a* spatial distribution in other temperate intertidal mudflats ecosystems adapted from Brotas, *et al.,* (1995)

Authors	Locality (Lat. N)	Chl.*a* Range	Author's conclusions Spatial	Temporal
Joint, 1978	S.W. England, 50° estuarine mudflat	top 0.5 cm seasonal: 25-80 $\mu g\ g^{-1}$		seasonal variation - max Apr./May. decrease due to sediment turnover by animal activity
Colijn & Dijkema, 1981	Dutch Wadden Sea, 53° Netherlands sand and mud flats	top 2 cm spatial: 30-110 mg m^{-2} seasonal: 10-240 mg m^{-2}	Chl. *a* corr. + with sed. particles $<16\ \mu m$	seasonal variation high values spr.-sum. negative effects of bad weather
Riaux, 1982	North Brittany, 48° France estuarine mudflat	top 0.5 cm spatial: 6-69 $\mu g\ g^{-1}$ seasonal: 25-250 mg m^{-2}	Chl. *a* corr + with % water of sediment	seasonal variation peaks in spr., aut., decrease in win. due to temperature & irradiance
Davis & McIntire, 1983	Netarts bay, 45° Oregon, U.S.A. estuarine flats	top 1 cm spatial: 46-94 mg m^{-2} seasonal: 10-130 (sand) 30-320 (silt)	Chl. *a* associated with sediment type and tidal height	seasonal variation max. spr. & aut., decrease in sum. caused by infauna
Shaffer & Onuf, 1983	Mugu Lagoon, 34° California, U.S.A sand and mud flats	top 0.5 cm spatial: 9-32 $\mu g\ g^{-1}$ seasonal: 5.50 $\mu g\ g^{-1}$	Chl. *a* > in fine sediments	seasonal variation high values spr.-sum.
Varela & Penas, 1985	Ria Arosa Spain, 43° sand flat	top 1 cm 25-100 mg m^{-2}		no clear seasonal trend max in Dec., Mar., Jul., Oct.
Present Study	Tagus Estuary, 38° Portugal estuarine flats	top 1 cm spatial: 11-240 mg m^{-2}, 1+-50 $\mu g\ g^{-1}$ seasonal: 20-300 mg m^{-2}, 5-75 $\mu g\ g^{-1}$	Chl. *a* corr. with fine sediments and tidal height	no clear seasonal variation max in sum.-aut. in upper sites max in win. in lower sites

From the table above we can observe that pooled chl-*a* range over different intertidal mudflat sites in temperate regions fluctuate spatially between magnitudes of 80mgm^{-2} to 320mgm^{-2}. Therefore, we can safely conclude that the model by Kromkamp was able to derive chl-*a* from remote sensing data since the derived chl-*a* ranges are within the ranges from other studies.

8.2. Evaluation of Land Surface Temperature over the Wadden Sea

Land surface temperature is the skin temperature of the earth's surface and it is one of the significant factors regulating microphytobenthic primary productivity in mudflats (Barranguet. *et al.*, 1998). Figure 8-2 shows land surface temperature (LST) results in degrees kelvin; retrieved from Landsat and Aster thermal bands over a period of five different years. From our investigations the cool colours in figure 8-2 indicate low temperatures whereas warm colours are an indication of high LST. It can be observed that warm temperatures are in areas with mudflats whereas cool temperatures are a characteristic of immersed areas. These temperatures vary spatially and temporally. The research findings also indicate that warmer temperatures were recorded on the 5th of October 2003 while cooler temperatures were received on the 13th of May 2000. In addition, investigations by Barranguet *et al.,* (1998) revealed an analogous trend of seasonal variability in LST over intertidal sediment surfaces.

Land surface temperature variability can as well be explained by the prevalence of seasonal differences, which are characterised by different weather conditions. Normally, during winter months we expect to have cool temperatures as well as warm temperatures in summer months. Intra-seasonal weather conditions are sometimes characterised with some days completely overcast with clouds or cloud free and this phenomenon can either suppress or increase LST. Therefore, this implies that the trend in LST derived over the Wadden Sea is expected and can be explained by the existing seasonal, diurnal differences in weather patterns.

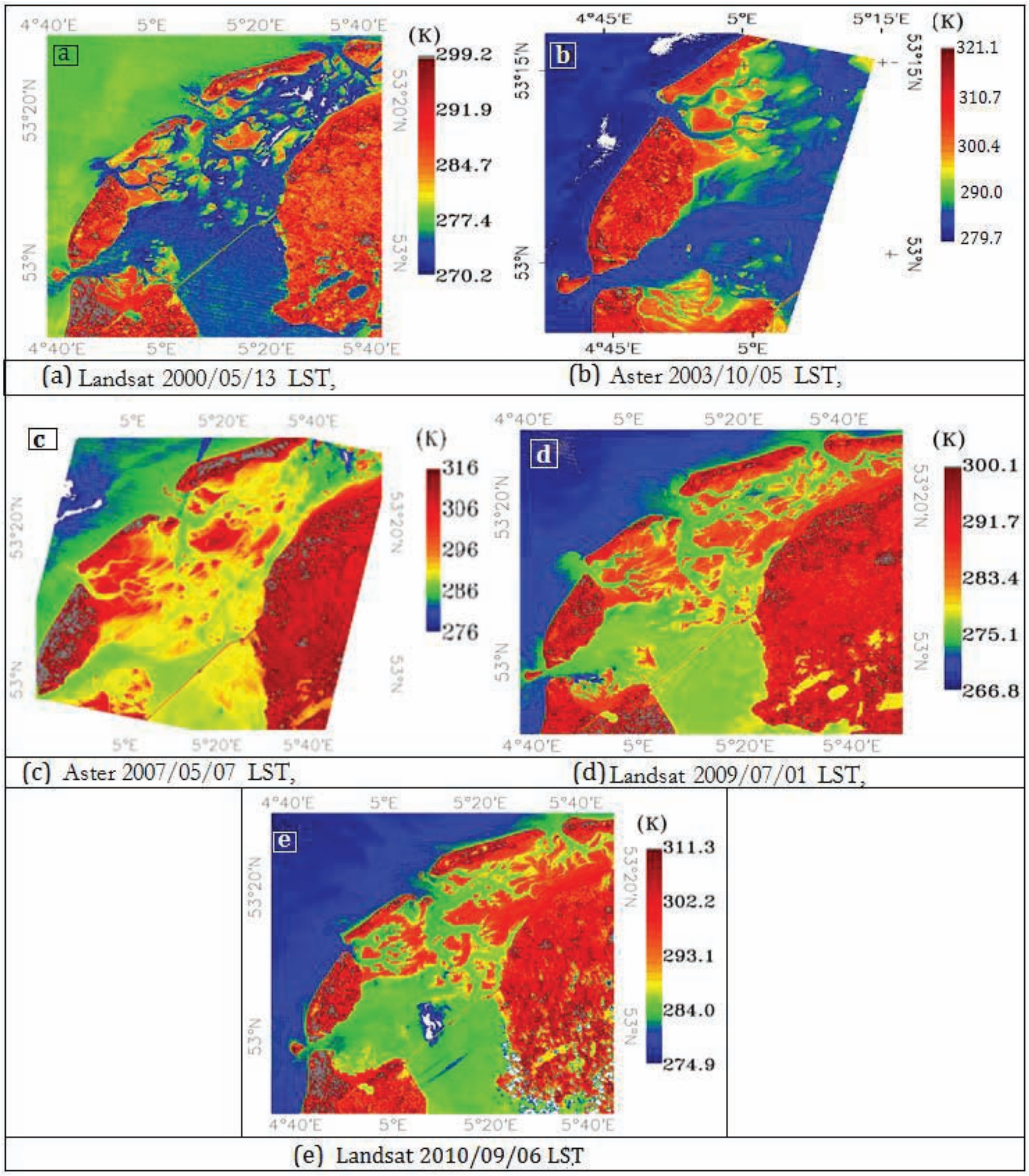

Figure 8-2: Land surface temperature retrieved from Aster and Landsat TIR bands

8.2.1. Relationship between P^B_{max} and Temperature

According Barranguet *et al.,* (1998) P^B_{max} is the maximum photosynthetic capacity at saturating irradiances and it is was one of the critical factors regulating microphytobenthic primary productivity. It is largely controlled by temperature. MacIntyre *et al.,*(1996) further stated that temperature has an effect on chl-*a* and P^B_{max}, which are the determinants of MPB primary productivity in mudflat sediments. Figure 8-3 demonstrates a linear relationship between P^B_{max} and the land surface temperature (K) with 0.71 R^2 value. It can be observed that P^B_{max} strongly increases with an increase in surface temperature. This trends is highly acceptable as surface temperature is one of the major determinants of primary productivity, more so this observation is consistent with the findings by Morris *et al.,* (2003). He found that P^B_{max} significantly increases with temperature until a temperature of approximately 30^{0}C is reached. However beyond 30^{0}C, P^B_{max} declines rapidly such that at 40^{0}C degrees a sharp decrease in photosynthesis is observed. However, Barranguet, (1997) has argued that although temperature has a significant influence on intertidal productivity, MPB primary productivity is much linked to light than temperature.

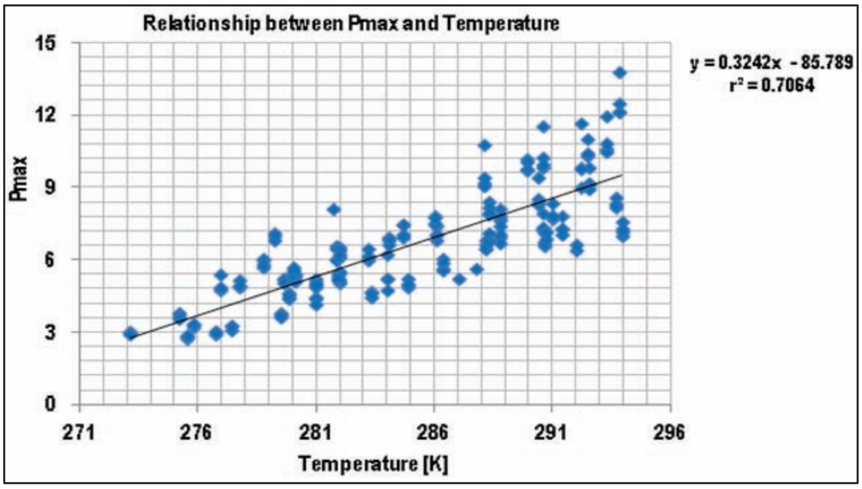

Figure 8-3: P^B_{max} versus land surface temperature [K].

The results from table 8-2 illustrate a summary of statistics for P^B_{max} derived from Landsat and Aster remote sensing datasets. Highest values of P^B_{max} were recorded in year 2000, with the least in 2010. The results seem to be within the range when compared to work by previous studies (Barranguet., *et al*., 1998; Kromkamp., *et al*., 1995). Barranguet., *et al.,* (2000), in his study found that maximum rates of carbon fixation (P^B_{max}) ranged between 2 and 18 mg C mg Chl-a^{-1}h^{-1} in three different sites on the intertidal flats in the Westerschelde and Oosterschelde estuaries.

Table 8-2: Statistical summary of P^B_{max} derived from remote sensing data over five year

		P^B_{max} [mg C chl-a^{-1}h^{-1}]			
Image	Date acquired	Min	Max	Mean	Stdev
Landsat	2000	4.81	19.22	10.11	1.77
Aster	2003	7.00	17.04	8.65	1.52
Aster	2007	3.09	16.22	8.77	1.75
Landsat	2009	5.93	15.13	9.03	1.18
Landsat	2010	6.41	13.18	8.63	0.58

8.3. Microphytobenthic Primary Productivity in the Intertidal Mudflats of the Wadden Sea

The results in figure 8-4 to figure 8-7 demonstrate microphytobenthic primary productivity maps from intertidal mudflats of the Wadden Sea area. From all the maps below, we will assume that cool colours depicts low MPB primary productivity whereas warm colours represents high primary productivity detected from Wadden Sea intertidal mudflats at a particular time and location. The model by Platt and Jassby, (1976) managed to capture the spatio-temporal distribution of MPB primary productivity in the

Wadden Sea. For example the distinction between intertidal mudflats areas of high and low microphytobenthic primary productivity has been clearly demonstrated from the findings. This distribution pattern varies from year to year and day to day. This observation can be attributed to a number of environmental factors such as light intensity, temperature differences, nutrient content variability and PAR (Morris *et al.,* 2003). However, for this study, the effect of PAR on spatio-temporal variability of MPB primary productivity is probably limited since the area is quite small. Most likely additional factors like temperature, light, nutrient content and sediment type can better explain the observed distribution. Literature shows that no consensus has been reached pertaining factors controlling MPB primary productivity in mudflats. According to Morris *et al.,* (2003) the effect of nutrients on MPB primary productivity is somehow limited but light and temperature have much influence on MPB primary productivity as they change rapidly on a seasonal, daily and hourly basis. On the other hand, Grant, (1986) has linked sediment transport in mudflat areas to the horizontal distribution of microphytobenthic diatoms, which considerably affect primary productivity. In actual fact, microphytobenthic primary productivity rates are determined by several factors, therefore, no single factor can be used as an explanation to the observed variability. Thus, integration of different factors can help understand the distribution of MPB primary productivity.

8.3.1. Effect of Kd and α^B on MPB Primary Productivity

The two variables have been used in testing the performance and limitations of the primary productivity model by Platt and Jassby, (1976). MacIntyre *et al.,* (1995) found that there is rapid attenuation of light in sediment surfaces. In his study he found that the attenuation ranged between 3.5 and 5.6 mm^{-1}. In testing the performance of the model, mean Kd and mean α^B; we increased initial by their standard deviations (fig 7.1) and then the effect of MPB primary productivity was assessed. From the results in figure 8-4 to figure 8-7 we found that when α^B; which is the photosynthetic efficiency increases, MPB primary productivity increases as well but for Kd it is total different for example, when Kd increase MPB primary productivity decrease. Kd is the attenuation of light intensity received by intertidal sediments surfaces. Therefore at deeper sediment levels the amount of light becomes limited for photosynthesis to take place as compared to the top sediment layer due to high attenuation effect by sediment properties.

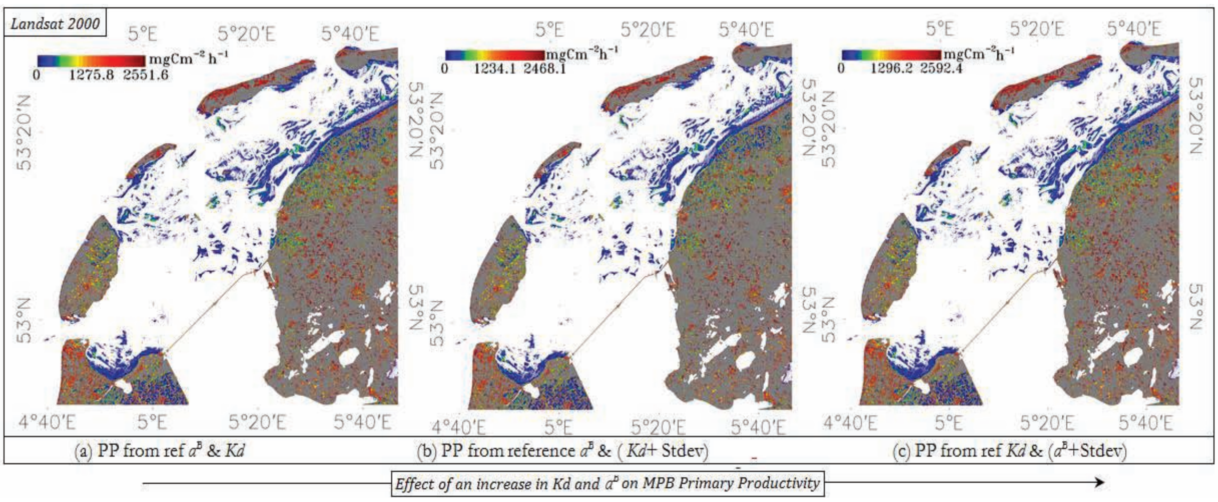

Figure 8-4: The effect of Kd (mm^{-1}) and α^B on MPB primary productivity in intertidal mudflats from Landsat ETM+ 2000

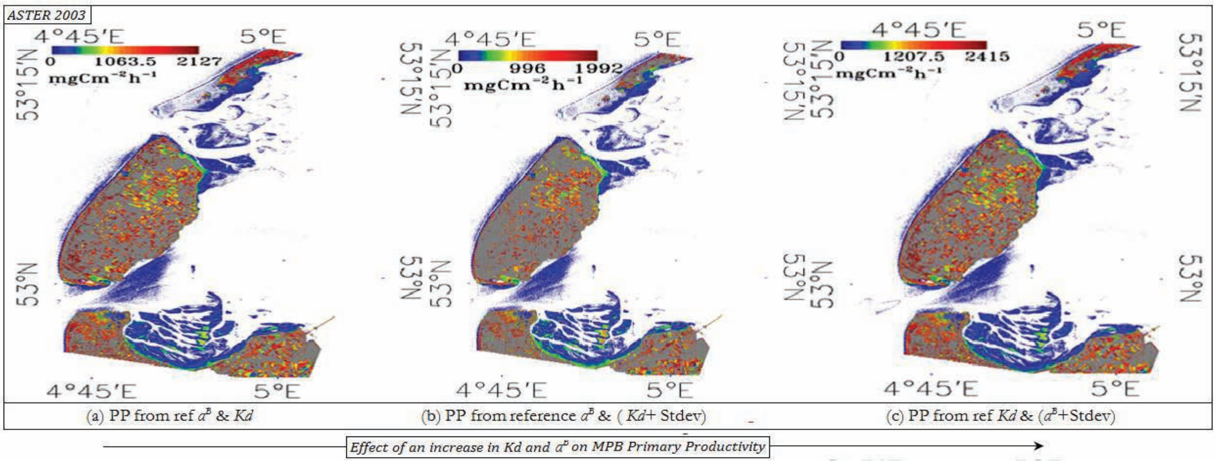

Figure 8-5: The effect of Kd (mm^{-1}) and α^B on MPB primary productivity in intertidal mudflats from Aster 2003

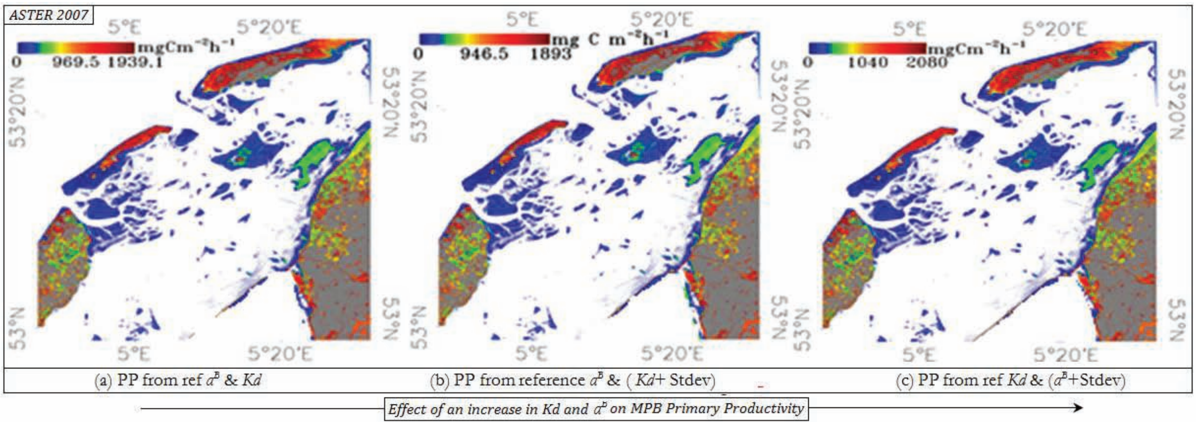

Figure 8-6: The effect of Kd (mm^{-1}) and α^B on MPB primary productivity in intertidal mudflats from Aster 2007

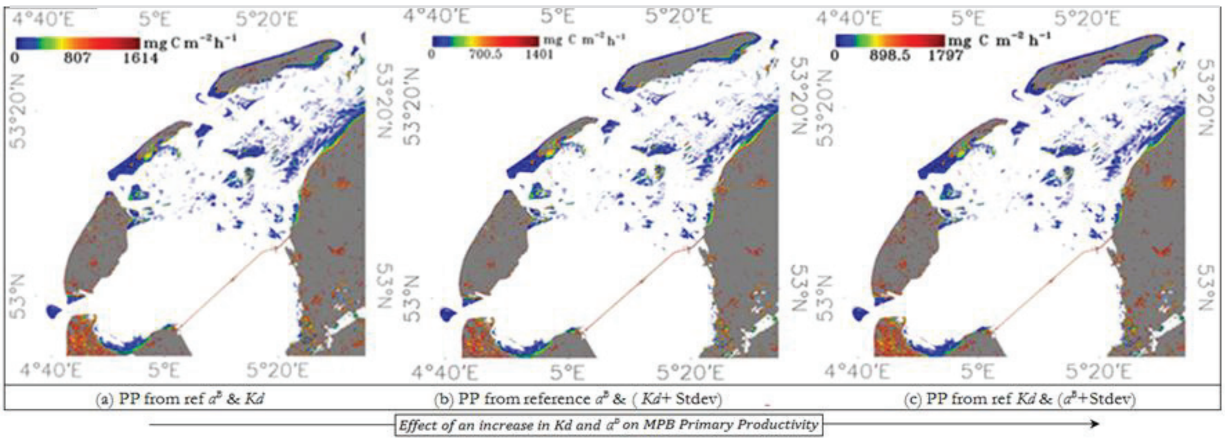

Figure 8-7: The effect of Kd (mm^{-1}) and α^B on MPB primary productivity in intertidal mudflats from Landsat TM 2009

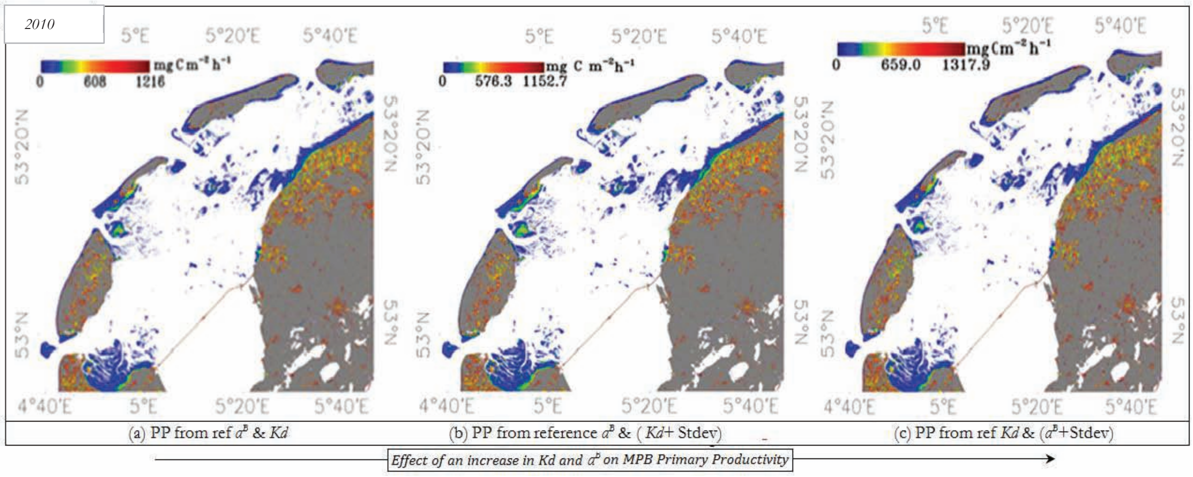

Figure 8-8: The effect of Kd (mm^{-1}) and α^B on MPB primary productivity in intertidal mudflats from Landsat TM 2010

8.3.2. The effect of Depth (Z mm) on Microphytobenthic Primary Productivity

Figure 8-8 demonstrates the effect of variability in depth on MPB primary productivity. It can be observed that at a vertical depth with a resolution of 2 mm, microphytobenthic primary productivity is very high when compared to vertical resolutions of 5 mm and 7 mm respectively. This observation implies that at the upper 0.2-2 mm (MacIntyre*., et al.*, 1996), the concentration of microphytobenthic diatoms is high as compared to deeper sediment depths. As a result, MPB primary productivity is bound to be more pronounced within the top sediment layer and decrease rapidly with increase in depth due to decreased rate photosynthesis. At depth beyond 2 mm light is the limiting factor. MPB primary productivity within vertical intertidal sediment profile is principally determined by light intensity. Literature has indicated that light varies significantly within the vertical sediment profile (MacIntyre*, et al.*, 1995). More so, the vertical distribution of MPB primary productivity depends on sediment characteristics. A study by Jesus *et al.,* (2006) has found that MPB biomass content decreased exponential in muddy sediments with a change in depth while in sandier sediments a uniform distribution was observed. According to MacIntyre, *et al.,* (1996) irradiance penetration in sediments is limited to the top layer approximately 2-3 mm and at this depth, photosynthesis occurs due to maximum illumination received. In summary, the results of this study have shown that the euphotic depth is one of the critical controlling factors regulating MPB biomass in intertidal sediment surfaces (Kromkamp*., et al.*, 2006).

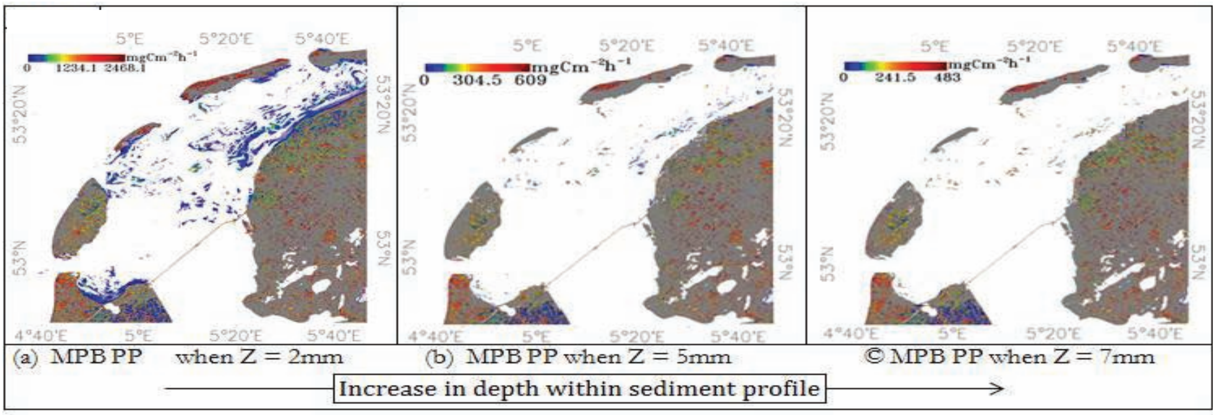

Figure 8-9: The effect of depth (mm) on MPB primary productivity in intertidal mudflats from Landsat ETM 2000

8.4. Comparison of Derived with Archived MPB Primary Productivity Findings

Derived MPB primary productivity results were compared with previous primary productivity concentrations findings since no validation was undertaken. Comparison of the results has indicated that the results of our study are within the normal concentration ranges expected. Figure 8-6 below illustrates the results of primary productivity concentrations results derived between 1991 and 2011 for different in the Wadden Sea and the ranges are between 0-10 $gCm^{-2}d^{-1}$. From the results a gradient in MPB primary productivity can be observed between 1991 and 2011, with high values recorded in 1991, 1993 and 1996 and the least in 2006 and 2011. When compared with MPB primary productivity derived from Landsat and Aster images it can also be observed that high primary productivity was in year 2000 and lower in year 2009. Therefore, similar MPB primary productivity rates can be observed between our study and the previous findings.

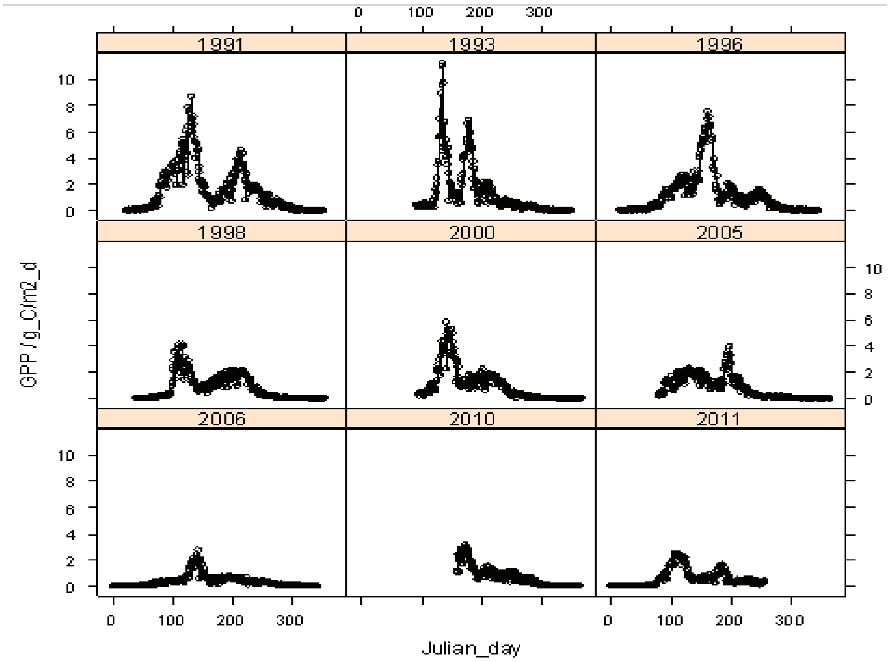

Figure 8-10: MPB primary productivity concentration derived from Wadden Sea, from (personal communication with Salama)

8.5. Possible Limitations

- Satellite remote sensing data provides only a snapshot of mudflat areas therefore they are greatly affected by the tide, making it difficult to derive sediment classes and MPB primary productivity over the area. Obtaining images acquired during a period of low tide was one of the major problems.
- MPB primary productivity results were not validated due complications in field measurements, but rather compared to other research findings on intertidal mudflats.
- The strength of field determined endmembers can be compromised by prevailing environmental factors like water content, mixed sediment properties and the presence of clouds during measurement period

9. CONCLUSIONS AND RECOMMENDATIONS

9.1. Conclusion

Microphytobenthic primary productivity was estimated from exposed intertidal mudflats using Landsat, and Aster images. To achieve this objective, supervised and imaged based classification methods were implemented using Spectral Angle Mapper (SAM) algorithm to characterize different sediment types in the Wadden Sea intertidal mudflats. The algorithm classified remote sensing data based on field derived endmembers and image extracted endmembers. In this thesis, an endmember is defined as a pure pixel spectral signatures determined from a single sediment type this being either sand or clay sediments Selection of the algorithm was done centered on the following advantages: (i) the algorithm is independent of brightness when dealing with remote sensing data, (ii) during classification, the algorithm is good at suppressing the adjacent effects concurrently enhancing different sediment spectral signatures (De Carvalho*, et al.,* 2000). On the other hand, MPB primary productivity in mudflat sediments was derived based on the model by Platt and Jassby, (1976). The model estimates MPB primary productivity using chlorophyll-*a* concentration ($mg.m^{-2}$), the maximum photosynthetic capacity at saturating irradiances (P^B_{max}), photosynthetic efficiency (α^B), light intensity (E_0), and sediment diffuse attenuation coefficient (Kd). Chl-*a*+ phaeopigments concentrations were derived from NDVI using equation by Kromkamp *et al.,* (2006). NDVI is a numerical indicator for biomass used as a proxy for estimating chl-*a* concentration from remotely sensed data. P^B_{max} was obtained from land surface temperature using the following mathematical model: y=0.3242x -85.789, with 0.71 R^2 value. E_0 was derived through following the Lambert beer law, whereas α^B was derived from field measurements. Finally, sensitivity analysis was done to assess the performance and limitations of the model through varying, α^B, Kd, and sediment euphotic depth. α^B, Kd, and sediment euphotic depth were used in assessing the model strength since they were considered to be the major determinants of microphytobenthic primary productivity on intertidal mudflat sediments.

Form the results, various spectral signatures were observed from different intertidal mudflat sediment types in the Wadden Sea. Spectral reflectances determined on clay sediments indicated the effect of chl-*a* absorption at 673 nm of the electromagnetic spectrum. Chl-*a* absorption at 673 nm was associated with the presence of microphytobenthic diatoms in clay sediments. In contrary, over sand sediments, a smooth spectral signature was observed with limited chl-*a* absorption at 673 nm, caused by the limited microphytobenthic content in sand sediments. Different intertidal mudflat sediment types we characterized from remote sensing data using SAM. Classified intertidal mudflat sediment classes varied spatially over the entire Wadden Sea, with sand sediments having a large aerial coverage than clay sediments. Also, based on observed supervised classification and image based classification results in this study, we can safely conclude that different intertidal mudflat sediment properties can be possibly derived from multispectral remote sensing data using SAM algorithm based on their inherent spectral characteristics.

Chl-*a*+phaeopigment concentration ($mg.m^{-2}$) were derived from Landsat (TM and ETM+), Meris and Aster remote sensing datasets using NDVI as a proxy for biomass. The findings indicate that chl-*a* + phaeopigments concentrations derived on intertidal mudflats ranged between 0 $mg.m^{-2}$ to 182 $mg.m^{-2}$, with the maximum attained in year 2000 and a minimum in year 2011. Further analysis of the results indicated that chl-a+ phaeopigments concentration distribution are similar to those of derived sediment classes (sand and clay), with more concentrations found in areas with clay sediments. This finding implies that an increase in sediment grain size, results in a decrease in the concentration of microphytobenthic diatoms which are responsible for chl-a+ phaeopigments in intertidal mudflats. This is expected because clay sediments are characterized by huge amounts microphytobenthic diatoms while sand sediments have limited of them. This observation can also be attributed to the fact that clay sediments are fine in nature and because of this they have high nutrient content and are largely cohesive. Therefore, the prevailing conditions make clay sediments conducive for colonization by microphytobenthic diatoms. On the other hand, sand sediments have a total different morphological structure, for example they are coarse grained, non- cohesive and they can easily be destabilized by tidal currents. These environmental conditions are not favorable for microphytobenthic inhabitation on sand sediments.

MPB primary productivity maps of the Wadden Sea have been derived from remote sensing data based on Platt and Jassby model. The results have indicated that the amount of microphytobenthic biomass within the vertical sediment profile largely rely on the incident irradiance, the diffuse attenuation coefficient (Kd) and depth (Z mm). It can also be concluded that microphytobenthic primary productivity vary spatial in the horizontal dimension on intertidal mudflat sediments. When compared to derived sediment classes, the distributions appear to resemble that of clay. In areas associated with sand sediments we again observed less primary productivity. Sensitivity analysis results have shown that MPB primary productivity on intertidal sediment surfaces was principally determined by α^B, Kd, and euphotic depth. When Kd was increased primary productivity decreased, whereas when α^B increased also did primary productivity. However, the effect of depth on primary productivity was clearly observed with high primary productivity recorded at 2 mm depth. At depth beyond 2 mm for example 5 mm and 7 mm an exponential decrease in primary productivity was observed. This observation is expected because in deeper sediment levels there is limited penetration by light. Microphytobenthic primary productivity in the vertical profile seems to be largely controlled by light which is an important component for photosynthesis to take place. According to MacIntyre, *et al.,* (1995) light intensity is a function of depth and it varies significantly within the vertical sediment profile. However, MPB primary productivity results from this study deserve to be handled with extra care because validation of the results was not done. The ranges of primary productivity concentrations derived from this study were only compared with other results and were found to be within the normal expected ranges.

9.2. Recommendation

To improve our understanding on the functioning of intertidal mudflat ecosystems there is need to:

- Develop an operational method that would help in deriving in-situ chl-*a* and MPB primary productivity concentrations which can be used to validate remote sensing estimates.
- For a better understanding of microphytobenthic primary productivity in the Wadden Sea, there is need to link the sediment diffuse attenuation coefficient of light (Kd) to intertidal sediment type and chl-*a*. The assumption is that clay sediments are cohesive for that reason they have higher Kd due to limited light penetration than sand sediments which are non-cohesive and largely affected by hydrodynamic processes that induce suspension, although the Kd is lower with increase in depth.

- To enhance the spectral purity of field determined endmembers through laboratory analysis to minimize the effect of the prevailing environmental factors (mixed sediment properties, water content etc.) and this would go a step further in improving intertidal sediment classification.

LIST OF REFERENCES

Abercrombie, M., Hickman, C. J., and Johnson, M. L. (1973). *A Dictionary of Biology*. Harmondsworth, UK: Penguin Books.

Acker, J. (1997). *SeaWiFS Data Available at the GSFC DAAC. backscatter*.

Adam, S., De Backer, A., De Wever, A., Sabbe, K., Toorman, E. A., Vincx, M., and Monbaliu, J. (2009). Bio-physical characterization of sediment stability in mudflats using remote sensing: A laboratory experiment. *Continental Shelf Research, 31*(10, Supplement 1), S26-S35.

Azab, M. A. (2012). *Integrating GIS, Remote Sensing, and Mathematical modelling for surface water quality management in irrigated watersheds*. Delft University of Technology Delft.

Bailey, S. W., and Werdell, P. J. (2006). A multi-sensor approach for the on-orbit validation of ocean color satellite data products. *Remote Sensing of Environment, 102*(1–2), 12-23.

Barranguet, C. (1997). The role of microphytobenthic primary production in a Mediterranean mussel culture area. *Estuar Coast Shelf Sci 44*, 753-765.

Barranguet., C., and Kromkamp, J. (2000). Estimating primary production rates from photosynthetic electron transport in estuarine microphytobenthos. *Marine Ecology Progress Series, 204*, 39-52.

Barranguet., C., Kromkamp, J., and Peene, J. (1998). Factors controlling primary production and photosynthetic characteristics of intertidal microphytobenthos. *Marine Ecology Progress Series, 173*, 111-126.

Barsi, J. A., S. J. Hook, J. R. Schott, N. G. Raqueno, and B. L. Markham,. (2007). *Landsat-5 thematic mapper thermal band calibration update*. Paper presented at the IEEE Geosci. Remote Sens. Lett.

Berk, A. G. P. A., P. K. Acharya, J. H. Chetwynd, L. S. Bernstein, E. P. Shettle, M. W. Matthew, and S. M. Adler-Golden, Hanscom AFB. (2000). MODTRAN 4 User's Manual. *MA: Air Force Res. Lab*.

Blanchard, G. F. (2000). The effect of geomorphological structures on potential biostabilisation by microphytobenthos on intertidal mudflats. *Cont. Shelf Res, 20*, 1243-1256.

Blanchard., G. F., Guarini, J. M., Gros P, and P, R. (1997). Seasonal effect on the relationship between the photosynthetic capacity of intertidal microphytobenthos and temperature. . *Journal of Phycology, 33*, 723-728.

Blanchard., G. F., and Montagna, P. (1995). Assessment of a brown tide impact on microalgal benthic communities in Baffin Bay (Texas) in 1990 using a primary production simulation model. *Oceanologica Acta, 18*, 371-377.

Boardman, J. W., and Kruse, F. A. (1994). *Automated spectral analysis: a geological example using AVIRIS data, North Grapevine Mountains, Nevada*. Paper presented at the Proceedings of the Tenth Thematic Conference on Geological Remote Sensing.

Brotas, V., Cabrita, T., Portugal, A., Serôdio, J., and Catarino, F. (1995). Spatio-temporal distribution of the microphytobenthic biomass in intertidal flats of Tagus Estuary (Portugal). *Hydrobiologia, 300-301*(1), 93-104.

Carrère, V., Spilmont, N., and Davoult, D. (2004). Comparison of simple techniques for estimating chlorophyll a concentration in the intertidal zone using high spectral-resolution field-spectrometer data. *Marine Ecology Progress Series, 274*, 31-40.

Chander, G., Brian L. Markham, and Helder, D. L. (2009). Summary of current radiometric calibration coefficients for Landsat MSS, TM, ETM+, and EO-1 ALI sensors. *Remote Sensing of Environment, 113 (2009)* 893-903.

Chaudhry, F., Chao-Cheng, W., Liu, W., Chang, C., and Plaza, A. (2006). Pixel purity index-based algorithms for endmember extraction from hyperspectral imagery. *Recent Advances in Hyperspectral Signal and Image Processing*.

Chein, I. C., and Qian, D. (2004). Estimation of number of spectrally distinct signal sources in hyperspectral imagery. *Geoscience and Remote Sensing, IEEE Transactions on, 42*(3), 608-619.

Clark, R. N., G. A. Swayze, A. Gallagher, T. V. V. King, and W.M. Calvin. (1993). *The U.S. Geological Survey, digital spectral library: Version 1: 0.2 to 3.0 microns*. Reston: U.S. Geol. Survey, , VA, .

Coll., C., Caselles, V., Sobrino, A., and Valor, E. (1994). On the atmospheric dependence of the split-window equation for land surface temperature. *International Journal of Remote Sensing, 15*, 105-122.

Coll., C., M, S. J., and Caselles, V. (2010). Validation of Landsat-7/ETM+ Thermal-Band Calibration and Atmospheric Correction With Ground-Based Measurements *IEEE Trans. Geosci. Remote Sens, 48*, 547-555.

CPSL. (2005). *Coastal Protection and Sea Level Rise: Solutions for Sustainable Coastal Protection in the Wadden Sea Region* Wilhelmshaven, Germany: Common Wadden Sea Secretariat (CWSS).

De Carvalho, and Meneses, P. R. (2000). Spectral Correlation Mapper (SCM): An Improvement on the Spectral Angle Mapper (SAM). *Summaries of the 9th JPL Airborne Earth Science Workshop: JPL Publication, 00-18*, 9

Delgado, M., de Jonge, V. N., and Peletier, H. (1991). Experiments on resuspension of natural microphytobenthos populations. *Marine Biology, 108*(2), 321-328.

Deronde, B., Kempeneers, P., and Forster, R. M. (2006). Imaging spectroscopy as a tool to study sediment characteristics on a tidal sandbank in the Westerschelde. *Estuarine, Coastal and Shelf Science, 69*(3-4), 580-590.

ESA. (2012). BEAM Earth observation toolbox and development platform. Retrieved 11 January, 2012, from http://www.brockmann-consult.de/cms/web/beam/

Fallah-Adl, H., J'aJ'a, J., S. Liang, Y. J. Kaufman, and J. Townshend. (1995). *Efficient Algorithms for Atmospheric Correction of Remotely Sensed Data, To appear in Proceedings Supercomputer 95*. Paper presented at the IEEE Computer Society Press.

Felde, G. W., G. P. Anderson, S. M. Adler-Golden, M. W. Matthew, and A. Berk. (2003). *Analysis of Hyperion Data with the FLAASH Atmospheric Correction Algorithm. Algorithms and Technologies for Multispectral, Hyperspectral, and Ultraspectral Imagery IX*. Paper presented at the SPIE Aerosense.

Franca., G. B., and Cracknell, A. P. (1994). Retrieval of land and sea surface temperature using NOAA-11 AVHRR data in north-eastern Brazil. *International Journal of Remote Sensing, 15*, 1695-1712.

Gillespie, A. R. (1985). *Lithologic mapping of silicate rocks using TIMS*.

Goetz, S. J., R. N. Halthore, F. G. Hall and B. L. Markham. (1995). Surface temperature retrieval in a temperate grassland with multiresolution sensors. *Journal of Geophysical Research, 100*(D12), 397-410.

Grant, J. (1986). Sensitivity of benthic community respiration and primary production to changes in temperature and light. *Marine Biology 90*, 299-306.

Green, A., Berman, M., Switzer, P., and Crai, M. D. (1988). A Transformation for Ordering Multispectral Data in Terms of Image Quality with Implications for Noise Removal. *IEEE Transactions on Geoscience and Remote Sensing, 26*(1), 65-74.

Guarini., J. M., Blanchard, G. F., Ph., G., and Harrison, S. J. (2010). Modelling the mud surface temperature on intertidal flats to investigate the spatio-temporal dynamics of the benthic microalgal photosynthetic capacity. *Marine Ecology Progress Series*.

Herman, P. M. J., J. J. Middelburg, and Heip, C. H. R. (2001). Benthic community structure and sediment processes on an intertidal flat: results from the ECOFLAT project. *Continental Shelf Research 21* 2055-2071.

Hofstede, J., Hähne, K., Oost, A., and Piontkowitz, T. (2005). *Human Activities*.

Hogan, C. M. (2011). Wadden Sea. *Encyclopedia of Earth. National Council for Science and the Environment. Washington DC*.

Hommersoms, A. (2010). *"Dense Water" and "Fluid Sand" Optical properties and methods for remote sensing of the extremely turbid Wadden Sea.* Vrije Universiteit, Amsterdam.

Hook, S. J., Gabell, A. R., Green, A. A., and Kealy, P. S. (1992). A comparison of techniques for extracting emissivity information from thermal infrared data for geologic studies. *Remote Sensing of Environment, 42*(2), 123-135.

IRWC. (2000a). *Sustainable Tourism Development and Recreational Use in the Wadden Sea Region*. Ribe County, Denmark.

Jesus, B., Brotas, V., Marani, M., and Paterson, D. M. (2005). Spatial dynamics of microphytobenthos determined by PAM fluorescence. *Estuarine, Coastal and Shelf Science, 65*(1–2), 30-42.

Jesus, B., Mendes, C. R., Brotas, V., and Paterson, D. M. (2006). Effect of sediment type on microphytobenthos vertical distribution: Modelling the productive biomass and improving ground truth measurements. *Journal of Experimental Marine Biology and Ecology, 332*(1), 60-74.

Johnson, B. R., and Young, S. J. (1998). *In-Scene Atmospheric Compensation: Application to SEBASS Data Collected at the ARM Site*.

Kalnay, E. M. K., R. Kistler, W. Collins, D. Deaven, L. Gandin, M. Iredell, S. Saha, G. White, J. Woollen, Y. Zhu, M. Chelliah, W. Ebissuzaki, W. Higgins, J. Janowiak, K. C. Mo, C. Ropelewski, J. Wang, A. Leetmaa, R. Reynolds, R. Jenne, and D. Joseph,. (1996) The NCEP/NCAR 40 year reanalysis project. *Vol. 77. Bull. Amer. Meteorol. Soc* (pp. 437-471).

Karsten, L., J B. EBlew, K. Eskildsen, K. Günther, B. Hälterlein, and Koffijberg., K. (2009). *Migratory Birds*. Wilhelmshaven, Germany.

Kaufmann, Y. J., A. E. Wald, L. A. Remer, B.C. Gao, R.R. Li, and L. Flynn. (1997). The MODIS 2.1-mm Channel-Correlation with Visible Reflectance for Use in Remote Sensing of Aerosol. *IEEE Transactions on Geoscience and Remote Sensing, 35*, 1286-1298.

Kealy, P. S., and Hook, S. J. (1993). Separating Temperature and Emissivity in Thermal Infrared Multispectral Scanner Data: Implications *IEEE Transactions on geoscience and remote sensing, 31*(6).

Kerle, N., Janssen, L., and Huurneman, G. C. (2004). *Princnples of Remote Sensing: An introductory textbook* (3rd edition ed.): he international Institute for Geo-Information Science and Earth Observation (ITC),.

Kromkamp, J. Morris, E. P., Forster, R. M., C.Honeywill, Hagerthey, S., and Paterson, D. M. (2006). Relationship of Intertidal Surface Sediment Chlorophyll Concentration to Hyperspectral Reflectance and Chlorophyll Fluorescence. *Estuaries and Coasts, 29* (2), 183-196

Kromkamp., J., and Forster., R. M. (2006). Developments in microphytobenthos primary productivity studies. In J. C. Kromkamp*, et al.* (Eds.), *Functioning of Microphytobenthos in Estuaries: Proceedings of the Colloquium* (pp. 9-30). Amsterdam: Royal Netherlands Academy of arts and Sciences, Nethelands Institute of Ecology (NIOO-KNAW).

Kromkamp., J., and Peene, J. (1995). Possibility of net phytoplankton primary production in the turbid Schelde Estuary (SW Netherlands). *Marine Ecology Progress Series, 121*, 249-259.

Kruse, F. A., Lefkoff, A. B., Boardman, J. W., Heidebrecht, K. B., Shapiro, A. T., Barloon, P. J., and Goetz, A. F. H. (1992). The spectral image processing system (SIPS)--interactive visualization and analysis of imaging spectrometer data. *Remote Sensing of Environment, 44*(2-3), 145-163.

Kruse, F. A., lefkoff, A. B., Boardman, J. W., Heidebrecht, K. B., Shapiro, A. T., Barloon, P. J., and Goetz, A. F. H. (1993). The Spectral Image Processing Systems (SIPS) - Interactive Visualisation and Analysis of Imaging Spectrometer Data. *Remote Sensing Environment*, 44

Lei, Z., Jianjun, W., Jie, Z., Feifei, Z., Ming, L., and Lin, Z. (2010, 25-30 July 2010). *Assessing the drought monitoring characteristic of timeseries NDVI indices in crop growing season.* Paper presented at the Geoscience and Remote Sensing Symposium (IGARSS), 2010 IEEE International.

MacIntyre, H. L., and Cullen, J. J. (1995). Fine-scale vertical resolution of chlorophyll and photosynthetic parameters in shallow-water benthos. *Marine Ecology Progress Series, 122*(227-237).

MacIntyre., H. L., Geider, R. J., and Miller, D. C. (1996). Microphytobenthos: The ecological Role of the "Secret Garden" of Unvegetated, Shallow- Water Marine Habitats.I Distribution, Abundance and Primary Production. *Jstor, 19*(2), 186-201.

Minor, T. B., Lancaster, J., Wade, T. G., Wickham, J. D., Whitford, W., and Jones, K. B. (1999). Evaluating Change in Rangeland Condition using Multitemporal AVHRR Data and Geographic Information System Analysis. *Environmental Monitoring and Assessment, 59*(2), 211-223.

Morris, E. P., and Kromkamp, J. C. (2003). Influence of temperature on the relationship between oxygen- and fluorescence-based estimates of photosynthetic parameters in a marine benthic diatom *(Cylindrotheca closterium). Eur. J. Phycol, 38*, 133 - 142.

Murphy, R. J., Underwood, A. J., Tolhurst, T. J., and Chapman, M. G. (2008). Field-based remote-sensing for experimental intertidal ecology: Case studies using hyperspatial and hyperspectral data for New South Wales (Australia). *Remote Sensing of Environment, 112*(8), 3353-3365.

NASA. (2002). MODIS - Aqua: Moderate Resolution Imaging Spectroradiometer. Retrieved 08/28/, 2011, from http://www.ioccg.org/sensors/aqua.html

Otto, S., and Zuidbroek, K. (2001). The Wadden Sea Region: A Unique Cultural Landscape.

Paterson, D. M., and Hagerthey, S. E. (2001). Microphytobenthos in Constrasting Coastal Ecosystems: Biology and Dynamics In K. Reise (Ed.), *Ecological Comparisons of Sedimentary Shores* (Vol. 151, pp. 105-125): Springer Berlin Heidelberg.

Pinckney, J., and Zingmark, R. G. (1991). Effects of tidal stage and sun angles on intertidal benthic microalgal productivity. *Marine Ecology Progress Series, 76*, 81-89.

Platt, T., and Jassby, A. D. (1976). The relationship between photosynthesis and light for natural assemblages of coastal marine phytoplankton. *Journal of Phycology, 12*, 421-430.

Prasad, A. K., Chai, L., Singh, R. P., and Kafatos, M. (2006). Crop yield estimation model for Iowa using remote sensing and surface parameters. *International Journal of Applied Earth Observation and Geoinformation, 8*(1), 26-33.

Prata, A. J. (1993). Land surface temperature from the advanced very high resolution radiometer and the along-track scanning radiometer. 1. Theory. . *Journal of Geographical Research., 98* 16 689-616 702.

Qin, Z., A. Karniel and P. Berliner. (2001). A mono-window algorithm for retrieving land surface temperature from Landsat TM data and its application to the Israel-Egypt border region. *international journal of remote sensing, 22*(18), 3719-3746.

Rahman, H., and Dedieu, G. (1994). SMAC: a simplified method for the atmospheric correction of satellite measurements in the solar spectrum *Int. J. Remote Sensing, , 15* (1), 123-143.

Reise., K., M. Baptist, P. Burbridge, N. Dankers, L. Fischer, and B. Flemming. (2010). *The Wadden Sea - A Universally Outstanding Tidal Wetland. Wadden Sea Ecosystem*. Germany: Wilhelmshaven.

Rouse, J. W., Haas, R. H., Schell, J. A., and D.W. Deering. (1973). Monitoring Vegetation Systems in the Great Plains with ERTS. Third ERTS Symposium. *NASA SP-, 351 I*, 309-317.

Rulinda, C. M., Wietske, B., and Stein, A. (2010). Image mining for drought monitoring in eastern Africa using Meteosat SEVIRI data. *International Journal of Applied Earth Observation and Geoinformation, 12, Supplement 1*(0), S63-S68.

Saltelli, A., Ratto, M., Andres, T., Campolongo, F., Cariboni, J., Gatelli, D.,.Tarantola, S. (2008). *Global Sensitivity Analysis*. The Primer: John Wiley and Sons.

Scheffer, M. (2001). *Ecology of shallow waters* (2nd ed.). Dordrecht: Kluwer Academic Publishers.

Schwengerdt, R. A. (1997). Remote Sensing: Models and Methods for Image Processing, p. 447.

Smith, G. M., Thomson, A. G., Moller, I., and Kromkamp, J. C. (2004). Using hyperspectral imaging for the assessment of mudflat surface stability. *Journal of Coastal Research, West Palm Beach (Florida). 20*(4), 1165–1175.

Stal, L. J. (2010). Microphytobenthos as a biogeomorphological force in intertidal sediment stabilization. *Ecological Engineering, 36*(2), 236-245.

Sundback, K., and Snoeijs, P. (1991). Effects of nutrient enrichment on microalgal community composition in a coastal shallow-water sediment system: an experimental study. *Bot. Mar, 34*, 341-358.

Sundback., K., and Jonsson, B. (1988). Microphytobenthic productivity and biomass in sublittoral sediments of a stratified bay, southeastern Kattegat. *Exp. Mar. Biol. Ecol, 122*, 63-81.

Trishchenko, A. P., Hwang, B., and Li, Z. (2002). *Atmospheric Correction of Satellite Signal in Solar Domain: Impact of Improved Molecular Spectroscopy*. Paper presented at the Twelfth ARM Science Team Meeting Proceedings, St. Petersburg, Florida.

Tucker, C. (1979). Red and photographic infrared linear combinations for monitoring vegetations. *Remote Sensing of Environment, 8*, 127-150.

Underwood, G. J. C., and J. Kromkamp. (1999). Primary Production by Phytoplankton and Microphytobenthos in Estuaries. . In N. D. B.*, et al.* (Eds.), *Advances in Ecological Research* (Vol. 29,, pp. 93-153): Academic Press.

UNEP. (2009). The Wadden Sea Germany and The Netherlands. Retrieved 24 August, 2011, from http://www.unep-wcmc-apps.org/sites/wh/pdf/Wadden_Sea.pdf

van der Wal, D., Herman, P. M. J., and Ysebaert, T. (2004). Space-borne synthetic aperture radar of intertidal flat surfaces as a basis for predicting benthic macrofauna distribution. *EARSeL eProceedings 3*, 69-80.

van der Wal., D., and Dool, W. (2010). Spatial Synchrony in Intertidal Benthic Algal Biomass in Temperate Coastal and Estuarine Ecosystems. *Ecosystems, 13*(2), 338-351.

YCEO. (2011). ASTER images: The Yale Center for Earth Observation. Retrieved 10 November, 2011, from http://www.yale.edu/ceo/

Young, S. J., B. R. Johnson, and J. A. Hackwell. (2002). An in-scene method for atmospheric compensation of thermal hyperspectral data. *Journal of Geophysical Research, 107*(D24), 4774.

Yuhas, R. H., Goetz, A., and Boardman, J. W. (1992). *Discrimination Among Semi-Arid Landscape Endmembers Using Spectral Angle Mapper (SAM) Algorithm, Summaries of the 4th Annual JPL Airborne Geoscience Workshop*. Paper presented at the AVIRIS Workshop.